Copyright Undertaking

This thesis is protected by copyright, with all rights reserved.

By reading and using the thesis, the reader understands and agrees to the following terms:

1. The reader will abide by the rules and legal ordinances governing copyright regarding the use of the thesis.
2. The reader will use the thesis for the purpose of research or private study only and not for distribution or further reproduction or any other purpose.
3. The reader agrees to indemnify and hold the University harmless from and against any loss, damage, cost, liability or expenses arising from copyright infringement or unauthorized usage.

IMPORTANT

If you have reasons to believe that any materials in this thesis are deemed not suitable to be distributed in this form, or a copyright owner having difficulty with the material being included in our database, please contact lbsys@polyu.edu.hk providing details. The Library will look into your claim and consider taking remedial action upon receipt of the written requests.

Pao Yue-kong Library, The Hong Kong Polytechnic University, Hung Hom, Kowloon, Hong Kong

http://www.lib.polyu.edu.hk

CONTROLLABLE DOPING AND ANISOTROPIC PROPERTIES OF TWO-DIMENSIONAL MATERIALS

XU KANG

M.Phil

The Hong Kong Polytechnic University

2018

The Hong Kong Polytechnic University

Department of Applied Physics

Controllable Doping and Anisotropic Properties of Two-dimensional Materials

XU KANG

A thesis submitted in partial fulfillment of the requirements for the degree of Master of Philosophy

August 2017

CERTIFICATE OF ORIGINALITY

I hereby declare that this thesis is my own work and that, to the best of my knowledge and belief, it reproduces no material previously published or written, nor material that has been accepted for the award of any other degree or diploma, except where due acknowledgement has been made in the text.

_______________________________ (Signed)

__________XU KANG_________ (Name of student)

Abstract

Two-dimensional (2D) materials are novel materials which have emerged during the last decade. Different from traditional three-dimensional (3D) materials, 2D materials can be thinned down to a single layer without surface dangling bonds. Because the interlayer interactions are weak van der Waals interactions. Due to their unique characteristics, 2D materials have applications in versatile electrical and opto-electrical devices. Novel physical phenomenon arising from 2D materials are interesting research topics.

MoS_2 is one type of 2D material which has been demonstrated to have broad applications in the future. Doping ultrathin MoS_2 by traditional ion-implantation is explored. A thin layer of Poly(methyl methacrylate (PMMA) is applied as a sacrificial layer to decelerate the dopant ions. Raman and transmission electron microscope (TEM) characterizations show that the PMMA layer protects the ultrathin MoS_2 flakes from being severely damaged by high-energy dopant ions. The p-doping effect of incorporated phosphorus ions on ultrathin MoS_2 have been demonstrated by photoluminescence (PL) and electrical characterizations. The doping effect can be tuned by controlling the thickness of MoS_2 flake and the thickness of PMMA layer.

Transitional metal oxides (TMO) are used to dope ultrathin MoS_2 by surface charge transfer. The oxide layers are deposited onto MoS_2 flakes by CMOS- compatible physical vapor deposition (PVD) methods. The modulation doping process introduces negligible damage of the MoS_2 lattice. PL and electrical characterizations are performed

to quantify the doping effects. TiO_2 and MoO_3 are found to have n- and p-doping effects on MoS_2, respectively. The doping level is comparable with other doping methods. The doping effect is dependent on the thickness of MoS_2.

AuSe is one type of material stacked by atomic chains with inter-chain van der Waals interactions. AuSe can be thinned down to the thickness of 2D atomic sheets like other 2D materials. The optical and electrical characterizations of α-AuSe are performed. AuSe is found to have strong anisotropic phonon vibrations by in-plane polarized Raman. Electrical characterizations of field-effect-transistor (FET) reveal the extraordinary high conductivity (σ_{2D} = 0.01 S) of carriers in AuSe. The metallic transport behavior of bulk AuSe is demonstrated by four-point resistivity measurement under low-temperature. Theoretical calculations of AuSe are performed. AuSe atomic chain is calculated to a semiconductor with an indirect bandgap of 1.26 eV while bulk AuSe is calculated to have no bandgap. Further experiments and calculations are required to fully understand the unique properties of AuSe.

List of Publications

1. Kang Xu, Yuda Zhao, Ziyuan Lin, Longyan Wang, Mansun Chen and Yang Chai, *Semicond. Sci. Technol.*, 2017, 32(12), 124002

2. Kang Xu, Yi Wang, Yuda Zhao, and Yang Chai, *Journal of Materials Chemistry C*, 2017, 5, 376-381

3. Yuda Zhao, Kang Xu, Feng Pan, Changjian Zhou, Feichi Zhou and Yang Chai, *Advanced Functional Materials*, 2016, 26(23): 4223-4230

4. Yuda Zhao, Jingsi Qiao, Zhihao Yu, Peng Yu,Kang Xu, Shu Ping Lau, Wu, Zhou, Zheng Liu, Xinran Wang, Wei Ji and Yang Chai, *Advanced Materials*, 2016, 29(5)

Acknowledgements

I would like to express my deep love for my parents and sisters and other family members. I would like to thank them for providing a warm and united family. I also very appreciate their firm support and trust on my personal decisions.

I would like to thank my supervisor, Dr. Yang CHAI, for his supervision, guidance and help during my stay in PolyU. Without his strong support, I would not be able to overcome all the confusions and difficulties during the last two years and finally accomplish this thesis.

I would like to give my special thanks for Dr. Yuda ZHAO, who has provided me selfless help and suggestions on the experiments. Without his help, I would not be able to setup and run my research so quickly and smoothly. I also appreciate all the beneficial discussions with Dr. Changjian ZHOU.

I would like to express my deep thanks for my peers and friends here in PolyU (including Ziyuan LIN, Feng PAN, Mengye WANG, Feichi ZHOU, Xinpeng SHEN, Fang YUAN, Lejuan CAI, Jingsi QIAO, Yao GUO *et.al*). It is their accompany that made me feel home here and supported me through all my depression hours. Their friendships are my most valuable memories afterwards.

Finally, I would like to thank Department of Applied Physics and PolyU for their supports all along.

Table of Contents

Abstract II
List of Publications IV
Acknowledgements V
Table of Contents VI
List of Figures VIII
List of Tables X
Chapter 1: Introduction 1
1.1 Background 1
1.2 Optical and Electrical-optical Properties of Monolayer Semiconductors 2
1.3 Objectives of Research 7
1.4 Outline of Thesis 8
Chapter 2: Controllable Doping of Ultrathin MoS_2 by Conventional Ion-implantation 9
2.1 Overview of Existing Doping Methods of 2D Materials 9
2.2 Introduction of PMMA-assisted Ion-implantation of MoS_2 11
2.3 Experimental Preparations 16
2.4 Results and Discussion of PMMA-assisted Ion-Implantation of MoS_2 17
2.4.1 Characterizations of MoS_2 Lattice after Implantation 17
2.4.2 Characterizations of Doping Effect 23
2.4.3 Implantation-Energy-Dependent Doping Effect 30
2.5 Summary 31
Chapter 3: Modulation Doping of Transition Metal Dichalocogenides/Oxides Heterostructure 33
3.1 Introduction 33
3.2 Experimental Preparations 34
3.3 Results and Discussion 35
3.3.1 Layer-dependent Negative Trion PL of 2D MoS_2 35
3.2.2 Layer-dependent n-doping of MoS_2 by Surface Charge Transfer from TiO_2 38
3.2.3 Layer-dependent p-doping of MoS_2 by MoO_3 47
3.4 Summary 51
Chapter 4. Optical and Electrical Characterizations of 2D AuSe 53
4.1 Introduction 53
4.2 Experimental Preparations 54
4.3 Experiment Results and Discussions 55
4.3.1 Geometrical and Electronical Structures of α-AuSe 55
4.3.3 Raman Spectra of α-AuSe 57
4.3.4 Electrical Transport Properties of α-AuSe 63

4.4 Summary 66
Chapter 5. Conclusions and Outlook 68
5.1 Conclusions 68
5.2 Outlook 71
References 73

List of Figures

Figure 1.1	Crystal structure, band structure and PL spectra of monolayer MoS_2.	3
Figure 1.2	PL spectra of monolayer MoS_2 versus the excitation energy.	5
Figure 1.3	Energy diagram representing photocarrier relaxation channels in monolayer and bilayer MX_2.	6
Figure 2.1	Introduction of Ion-implantation technology.	13
Figure 2.2	PIII-assisted Ion-implantation of few-layer MoS_2.	15
Figure 2.3	Schematic of PMMA-assisted ion-implantation and TEM characterizations.	19
Figure 2.4	Raman characterizations of MoS_2 after ion-implantation.	22
Figure 2.5	PL characterizations of MoS_2 after ion-implantation.	27
Figure 2.6	Electrical characterizations of MoS_2 FET.	29
Figure 2.7	Implantation energy dependent doping effect.	31
Figure 3.1	Layer-dependent PL analysis of ultrathin MoS_2 flakes.	38
Figure 3.2	PL spectra of ultrathin MoS_2 flakes before and after depositing 6-nm-thick TiO_2	40
Figure 3.3	Raman spectra of 1-4L MoS_2 before (black line) and after (red line) 6-nm-thick TiO_2 doping.	41
Figure 3.4	PL and Raman spectra of 1L-3L MoS_2 before and after being doped with 30-nm-thick TiO_2.	43

Figure 3.5	Electrical characterizations of MoS_2 FET for n-doping by TiO_2.	45
Figure 3.6	DFT simulation results of the n-doping process and band structures of MoS_2 and TiO_2.	47
Figure 3.7	PL spectra of ultrathin MoS_2 flakes before and after being doped by 6-nm-thick MoO_3.	48
Figure 3.8	Electrical characterizations of MoS_2 FET for p-doping by MoO_3.	50
Figure 3.9	DFT simulation results of the p-doping process and band-structures of MoS_2 and MoO_3.	51
Figure 4.1	Theoretical calculation results of geometrical of α-AuSe.	56
Figure 4.2	TEM characterizations of AuSe.	57
Figure 4.3	Raman spectra of AuSe.	59
Figure 4.4	Polarization of peak B and peak C.	61
Figure 4.5	Low-temperature Raman spectra of bulk AuSe.	62
Figure 4.6	Calculations and characterizations of the electronic structure of AuSe.	64
Figure 4.7	Four-point electrical characterizations of AuSe	66

List of Tables

Table 4.1 Calculated vibration modes of AuSe. 58

Chapter 1: Introduction

1.1 Background

Two dimensional (2D) materials are layered materials with strong intralayer chemical bonding and weak interlayer van der Waals interactions. Different from traditional bulk materials, 2D materials can be thinned down to the thickness of a few layers without surface dangling bonds. Since the first report of graphene in 2004, 2D materials have been under hot research due to their unique electrical, optical and optoelectrical properties.

To increase the working frequencies of transistors, the channel length of transistors need to be scaled down. However, for traditional bulk materials, their scaling has reached the limitation due to the arise of short-channel effects. Side-effects arise when the channel length is decreased to the same magnitude as the depletion region of source and drain, *i.e.*, drain-induced barrier lowering (DIBL), surface scattering, velocity saturation, *etc*.[6] Due to the ultra-small surface energy and the lack of surface dangling bonds, 2D materials have strong immunity for short-channel effects.[1] This characteristic makes 2D semiconductors promising materials to replace silicon in the future semiconductor industry.

Beside from the semiconductor industry, 2D materials have broad applications in versatile electrics and opto-electrics. Graphene and PtX_2 (X = S,

Se) are 2D materials with extraordinary high (σ_{2D} = 0.1 S) conductivity. They can be used to replace the metal contacts or inter-connects in the future electronics to lower metal-semiconductor contact barriers or scale down the dimension of circuits.[3,7,8] Some 2D materials (*i.e.*, MoS_2) have bandgaps that lay in the near-infrared region and have strong light-matter interaction, which makes them interesting materials to study for photodetectors. Another type of 2D materials like black phosphorus[9] and ReS_2[8] possess high in-plane asymmetry, which leads to strong anisotropic electrical and opto-electrical properties.

On the other hand, interesting physics phenomenon (excitons,[10] valleytronics,[11] quantum transportation[12]) have emerged from the research of 2D materials. Study and modulate the properties of 2D materials is an interesting and promising research topic to conduct.

1.2 Optical and Electrical-optical Properties of Monolayer Semiconductors

Despite the ultra-small thickness of two-dimensional transitional metal dichalcogenides (TMDs) materials, such as monolayer or bilayer MX_2 from group 6, they have very large absorption (5% - 10%)[13] and emission of light in the visible light region (bandgap = 1-3 eV). Recent studies about the optical properties of these materials (*i.e.*, band-gap photoluminescence,[14] valleytronics,[15] tightly bound trions[16] *etc.*) and distinctive electrical properties of these materials have shed light on their potential applications on optoelectronics. Recent *ab initio* studies have attributed the strong light-matter interaction in ultrathin TMDs to 'band-nesting'. In the band-nesting region, the conduction band and valence band is parallel to each other, which gives rise to the singularity feature of the Joint Density of States

(JDOS). The JDOS diverges for resonance energy, which great enhances the optical conductivity.[17]

For monolayer MX_2, the conduction band minimum and the valence band maximum are both located at the K/K′ point of the Brillouin zone (**Figure 1.1**). Conduction band valley at the Λ point and the valence band hill at the Γ point play a dominant role in the direct to indirect gap crossover. Band-nesting regions in Mo and W disulphide and diselenide monolayers occur midway between the Γ and Λ points.

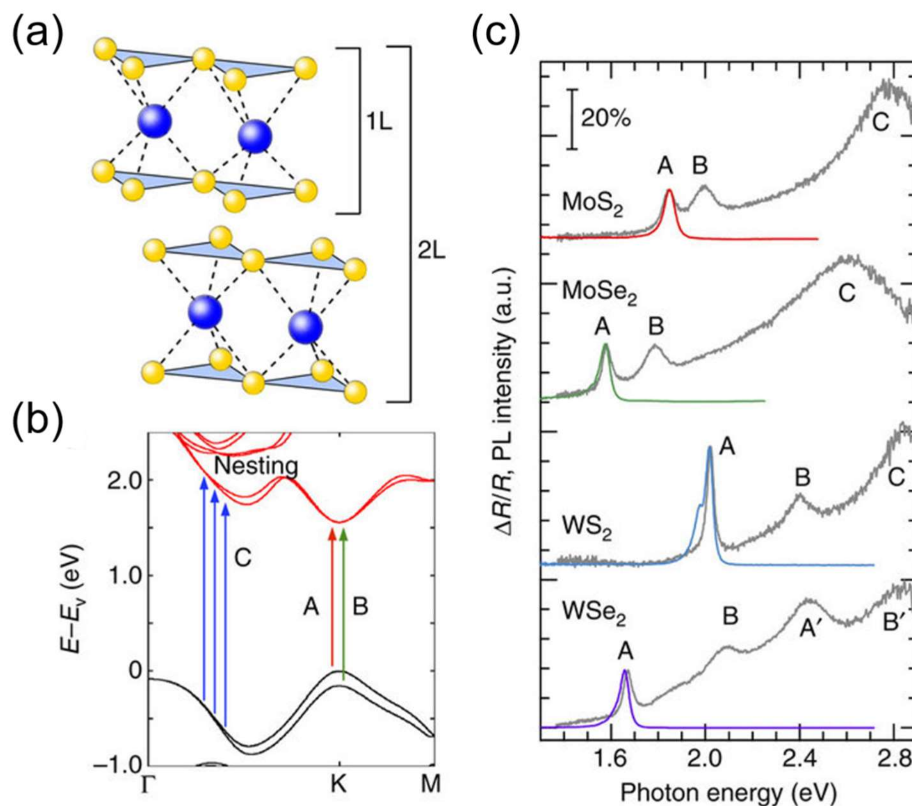

Figure 1.1 Crystal structure, band structure and PL spectra of monolayer MoS_2. (a) Lattice structures of monolayer and bilayer MX_2. (b) The band structure of

monolayer MoS_2. The arrows indicate the transition in A, B and the band nesting. (c) PL spectra (red, green, blue and purple curves) from excitation at the C (A' for WSe_2) peak and differential reflectance spectra (grey curves) of monolayer MX_2 flakes on quartz substrates.[18]

The absorption spectra, photoluminescence excitation (PLE) spectra and relative Quantum Yield (QY) of emission of monolayer MX_2 have been collected and compared. It is found that the PLE intensity of A exciton peak is enhanced at the resonance of B absorption peak. While for exciting energy higher than B exciton, although the absorption of C peak is very strong, the PLE intensity of A exciton peak is small or only weakly enhanced. The weak PLE intensity at the resonance of C peak is ascribed to the effective and fast (< 500 fs) separation of electrons and holes in the band-nesting region. To verify this effect, the same characterizations of bilayer MX_2 are performed. The absorption spectra of bilayer MX_2 is similar with that of monolayer MX_2. However, different from monolayer MX_2, bilayer MX_2 exhibits indirect bandgap feature. Bilayer MX_2 exhibit indirect band gap emission involving Λ valley in the conduction band and Γ point in the valence band. The band-nesting region is between Λ point and Γ point. So, large portion of excited carriers in the band nesting region are expected to relax to the Λ point and Γ point. So, the QY of indirect band gap emission is expected to be greatly enhanced when the exciting energy resonances with the C absorption peak. To demonstrate this, the QY of indirect emission and direct emission are compared. It is found that the I/A ratio is positively proportional to the exciting energy, which is consistent with theory explanation. These results demonstrate that the

photocarrier relaxation pathways and radiative combination channels are closely related to the band-nesting feature.

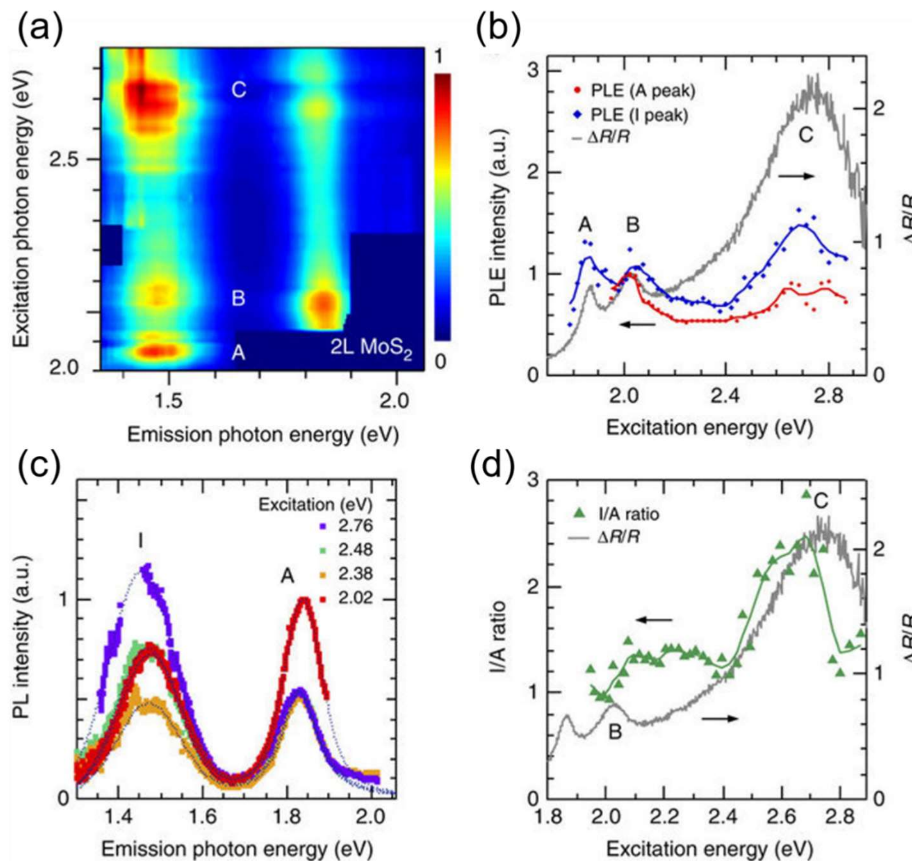

Figure 1.2 PL spectra of monolayer MoS_2 versus the excitation energy. (a,b) PLE intensity map and PLE spectra for bilayer MoS_2. (c) PL spectra of MoS_2 collected with different excitation energy. (d) The ratio of integrated PL intensity between the I and A peak versus the excitation energy. The differential reflectance spectrum is also shown for comparison.[18]

Based on these results, Eda *et al.* proposed photocarrier relaxation pathway models when the excitation energy is in resonance with the band nesting energy for monolayer and bilayer MX_2, respectively.[18] In monolayer

MX_2, a large fraction of photoexcited carriers generated in the band-nesting region relax to the Λ valley and Γ hill. Radiative recombination at this state competes with non-radiative decay and intra-band scattering to lower energy state K/K'. So only a small fraction of carriers is transferred to the K/K' state while direct band gap emission is occurred. In bilayer MX_2, a moderate fraction of photo-generated carriers relaxes to the Λ valley and Γ hill. Strong light-matter interaction of TMDs materials make them promising candidates for opto-electronic applications. The PL characteristic of TMDs is a complex process, which is dependent on the intrinsic energy band structure and external excitation energy.

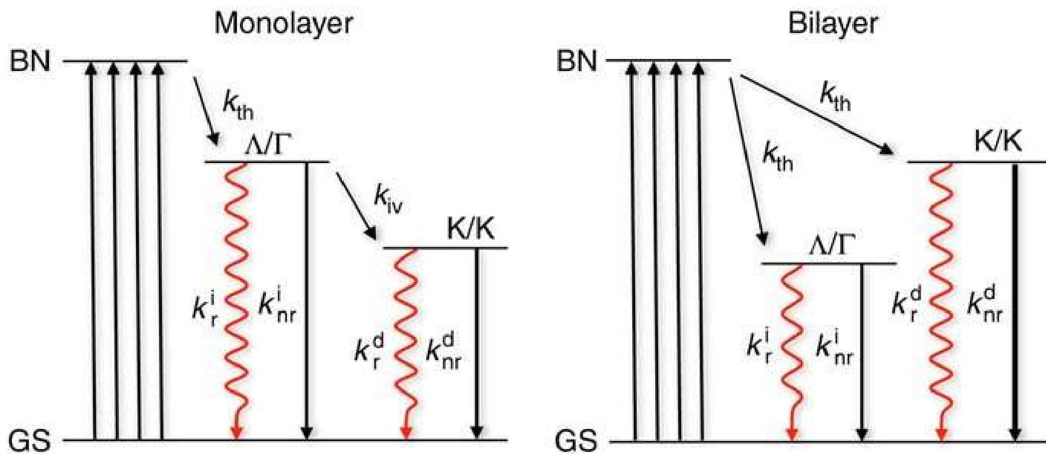

Figure 1.3 Energy diagram representing photocarrier relaxation channels in monolayer and bilayer MX_2. The initial excitation is from the ground state (GS) to the band nesting (BN) energy.[18]

1.3 Objectives of Research

Though 2D materials have been demonstrated to be promising building blocks for the next generation circuits. Effective doping methods for 2D materials remain as an open challenge. Controllable modulation of carrier density and carrier type is essential for the realization of complementary logic circuits in the future. On the other hand, the interaction between carrier and exciton enables additional path to modulate the photoluminescence (PL) of 2D materials. Exciton-dominant and trion-dominant PL of 2D material can be switched by n- or p-doping. In this study, the updated research status of doping 2D materials is reviewed. The objective is to explore possible doping methodologies for 2D materials. Optical and electrical properties of 2D materials are used to characterize the doping effects. Meanwhile, the doping methods are also used to tailor the optical and electrical properties of 2D materials.

AuSe in one type of crystal stacked by atomic chains with van der Waals interactions. The unique crystal structure of AuSe enables it to be thinned down to a highly-anisotropic 2D atomic sheet. However, there has been rare study about AuSe since its first report in 1976. [19] In this study, we aim to study the 2D form of AuSe. By theoretical calculations and experiments, we aim to reveal the phonon vibrational modes of AuSe, exploit its in-plane anisotropy and electrical transport characteristics, etc. This study could deepen our understanding about AuSe and other materials with similar crystal structure. Also, AuSe could find its applications in various electrical devices in the furure.

1.4 Outline of Thesis

This thesis is organized as follows. Chapter 1 is the introduction of this thesis. The fundamental properties of 2D materials are introduced in this chapter. Chapter 2 introduces the study of doping 2D MoS_2 utilizing the traditional ion-implantation method, with the assist of organic sacrificial layer. This part shows that it is possible to use traditional ion-implanter to dope 2D materials directly in a controllable manner. Also, the reported doping methodologies of 2D materials are reviewed briefly in this chapter. Chapter 3 introduces the study of doping 2D MoS_2 by oxide layer modulation doping. This doping method has negligible damage to the host materials and is CMOS-compatible. The study of 2D AuSe is introduced in Chapter 4, including theoretical calculations and experiments about geometric and electronic properties of AuSe. Chapter 5 concludes this thesis and gives outlooking for future works.

Chapter 2: Controllable Doping of Ultrathin MoS_2 by Conventional Ion-implantation

2.1 Overview of Existing Doping Methods of 2D Materials

In conventional silicon based semiconductor industry, the carrier type and carrier density in semiconductors are modulated by thermal diffusion and ion-implantation. These effective doping methods are necessary for the realization of complementary circuits. Emerging 2D materials are promising materials for the next generation circuits. Due to the ultrathin nature of 2D materials, traditional doping methods cannot be applied directly to them. Developing effective doping methods for 2D materials are of essential importance. Various doping methods have been explored by many research groups and they are introduced in this section.

Chemical vapor deposition (CVD) is a promising method to realize the large-scale growth and application of 2D materials. Solid sources are evaporated at high temperature to synthesis 2D materials. By controlling the composition of precursors, the elemental composition of synthesis 2D material can be modified. The carrier density and carrier type of the synthesis 2D material can be well-controlled. [20 -22]

Ion-implantation is a mature and widely-used doping method in the modern silicon-based semiconductor industry. The dopant profile, carrier density and carrier type in the host material can be well-controlled by ion-implantation to achieve desired doping effect. Thus, ion-implantation meets the desire for doping 2D materials in a controllable and large-scale manner. However, this technology cannot be applied directly to dope 2D materials. Due to the ultrathin nature of 2D materials, high-energy dopant ions can cause severe damage to the crystal structure and has very low retention. By low-energy ion-implantation, the incorporation of various dopants into graphene or MoS_2 has been studied and realized. [23-28] However, traditional ion-implanters are not capable of low-energy implantation. The lowest implantation energy of traditional implanters is ~ 1 keV, which is much larger than the ultralow energy (< 50 eV) required in similar reports.

Plasma treating the surface of 2D materials has been demonstrated to be effective doping methods. MoS_2 flakes and graphene have been demonstrated to be effectively-doped by this method. [29-32] Although plasma treating serves an effective way to dope 2D materials in a CMOS-compatible and large-scale manner, there are some challenges in their practical application. First, unintended etching of 2D material surface is an issue of plasma treating. Second, it is hard to modify the dopant profile in a well-controllable way.

Substitutional doping or surface plasma treatment can inevitably result in defects in 2D materials. The defects become scattering centers for electrons, thus degrading the mobility of carriers in electrical devices. On the other hand, modulation doping provides a mean to modulate the carrier density in the host

material without causing damage to the lattice structure. 2D materials are extremely sensitive to surface gas adsorption because of large surface area and ultrathin body thickness. Gas molecules are found to have doping effect on 2D materials and 2D materials have been explored for their application in gas sensors and gas filters. [33-37] Similar with gas molecules, organics have also been demonstrated to be doping effects on common 2D materials. [38-46] Different from gas molecules and organics, oxide dopants are stable in ambient and compatible with CMOS technology. The doping effect of oxide layers is originated from the energy difference between the fermi level of 2D material and the work function of oxide layers. [47,48] The doping effect of the oxide layer is mainly dependent on the work function of the oxide layer. High-work function oxides usually have p-doping effect (WO_x and MoO_x); [47 49] low-work function oxides usually have n-doping effect (TiO_x and ZnO_x). [48,50] Also, the oxygen vacancies in oxide layers can change the work function of oxide layers and thus modifying the doping effects of oxide layers. [49,50] Oxide xide layers are deposited by physical vapor deposition (PVD) or chemical vapor deposition (CVD). These deposition procedures are CMOS-compatible. By choosing specific oxide specie and modifying the deposition parameters, desired doping effects can be achieved.

2.2 Introduction of PMMA-assisted Ion-implantation of MoS_2

The existing doping methods (*i.e.*, surface adsorption, substitutional doping during growth *etc.*) have been proven to be effective in tuning the carrier type or carrier concentration in 2D materials. However, some of them are incompatible with CMOS technology and have not taken the most advantage of the established

semiconductor facilities.

Ion-implantation is a material engineering process, in which ions are accelerated in an electrical filed and impacted into the body of a target material (**Figure 2.1**). This process is used to change the electrical, optical, chemical or structure characteristics of a target material. Specified ions are impacted into the target materials and stopped there. Implanted ions can change the elemental composition of the target material if they are not composition of the target material. Accelerated ions can damage or even destroy the structure of a target material if the acceleration of the ions is high enough. Ion-implantation can modify the properties of a target material in a controllable manner, and is a well-established and widely-used doping technology in the current semiconductor industry. It is used to modify the carrier type (electron-dominate or hole-dominate) or carrier concentration in a target semiconductor material. The dopant profile and dopant depth could be easily tuned by implantation energy and implantation fluence.[51] For traditional silicon based semiconductors, this technology is well-established and optimized during the past decades. But for novel 2D materials, this technology has not been explored yet. If this technology is to be replaced by new technologies or facilities, the cost for the semiconductor industry is remarkably high. On the other hand, directly transplanting this technology to 2D materials can minimize the cost while maximize the effectiveness.

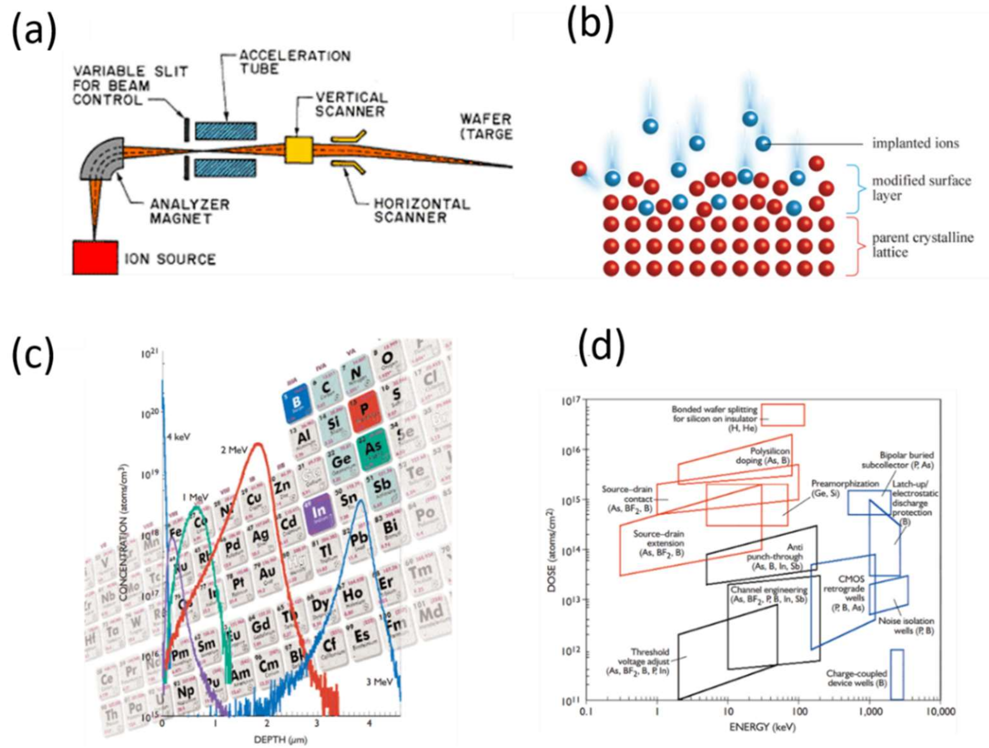

Figure 2.1 Introduction of Ion-implantation technology. (a) Schematic of the setup an implanter. [52] (b) Cross-sectional schematic of ion-implantation process. [53] (c) Typical dopant depth, dopant profile and dopant species. (d) Summary and comparison of the doping energy and dopant dose of different dopant species. [54]

However, the implantation energy of conventional implanters is too high (> 10 keV) for 2D materials. High energy dopant ions can damage or even destroy the crystal structure of ultrathin 2D materials. Since the thickness of few-layer 2D materials is in the order of a few nanometers, the retention of dopant ions in the body of 2D materials is very low.[55] To circumvent the problems arose from the high energy characteristic of traditional implanters, researches have been focusing on the modifications or replacements of present implanters to meet the requirements for doping 2D materials. For example, A. Nipane *et.al* introduced

CMOS compatible plasma immersion ion-implantation (PIII) into the implantation process for MoS_2 (**Figure 2.2**).[56] The ionized plasma atmosphere decelerates the dopant ions before they reach 2D materials. The decelerated ions have a high retention inside MoS_2 and do not result in serious damage to MoS_2 lattice. By using this doping strategy, ambipolar MoS_2 FET has been successfully fabricated. This method can be combined with polymer mask to selectively dope MoS_2. However, some drawbacks are inevitable with this strategy. First, modifications of traditional implanters are required to support PIII. These modifications usually cost high and may not be compatible with all the implanters. Then, plasma can lead to unintended etching of 2D materials in the horizontal directions. Given the ultra-small thickness of few-layer MoS_2, unintended etching can result in obvious yet unexpected change in the characteristics of MoS_2. Third, the dopant depth and dopant profile is hard to manipulate with the existence of plasma atmosphere.

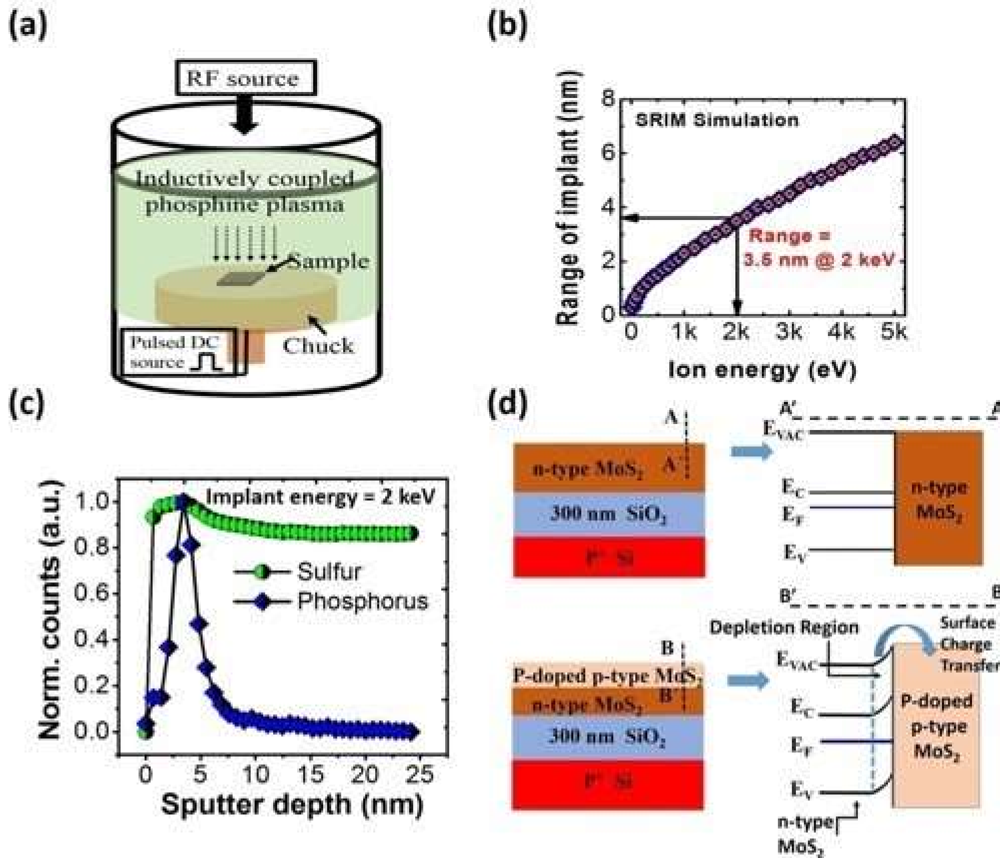

Figure 2.2 PIII-assisted Ion-implantation of few-layer MoS_2.[56] (a) Illustration of the setup of PIII-assisted Ion-implantation process. (b) Simulated dopant depth versus doping energy. (c) Measured dopant profile of phosphorus implantation. (d) Cross-section schematics and energy band diagrams illustrating the impact of phosphorus p-doping the top few layers of MoS_2.

Ultra-low energy implanters have been explored to dope 2D materials.[24-27] Nitrogen, Boron and Fluorine ions are successfully incorporated into Graphene lattice utilizing ultra-low energy implanters.[25] TEM pictures show only small damage to graphene lattice during the implantation process. But most of the implantation energies are below 100 eV, which is far beyond the capability of conventional high energy implanters. It is clearly not cost-effective to replace all

conventional implanters by ultra-low energy implanters. Thus, a feasible, CMOS compatible and effective implantation method of 2D materials is required.

Here we report a method to directly utilize traditional ion-implanter to dope 2D materials. A thin layer (200 nm or 1000 nm) of Poly(methyl methacrylate) (PMMA) is spin-coated onto ultrathin MoS_2 flakes as a sacrificial layer. The PMMA layer decelerates the dopant ions and successfully retains a portion of dopant ions inside the 2D MoS_2 flakes. Phosphorus is selected as the dopant since it has one electron less than sulfur so it has p-doping effect on MoS_2. It has high affinity for molybdenum in sulfur-deficient MoS_2 so it is easy to be incorporated into MoS_2 lattice.[32] Phosphorus ions were implanted with implantation energies varying from 10 keV to 40 keV and a fluence of $5x10^{13}$ cm^{-2}. The PMMA layer was then easily washed away by Acetone and Isopropyl alcohol (IPA) after the implantation process. Raman spectra and High Resolution TEM (HRTEM) show that there is no obvious damage to the MoS_2 lattice. Photoluminescence (PL) and electrical characterizations show that few-layer MoS_2 flakes are successfully p-doped by incorporated P atoms. Furthermore, the doping effect can be tuned by the thickness of PMMA layer. This doping strategy is compatible with state-of-the-art CMOS technologies and can be used for large-scale manufacturing.

2.3 Experimental Preparations

Single crystals of MoS_2 are purchased from commercial producer (2D Semiconductors). Scotch tape assisted mechanical exfoliation method is used to transfer ultrathin MoS_2 flakes onto target substrates (300-nm-thick SiO_2/Si wafer). Ultrathin flakes (< 10 nm) of MoS_2 are identified under optical microscope by

contrast. The thickness of MoS_2 samples are measured by Atomic Force Measurement (AFM). Before implantation, PMMA is spin-coated onto the samples by a Sawatec Spin Coater SM-180-BT. The spin-coated PMMA is then baked at 180 °C for 1 min. The thickness of PMMA is measured by a DektakXT Surface Optical Profiler. For PMMA spin-coated at a rate of 4kr/s for 30s, the thickness was measured to be 200 nm; for PMMA spin-coated at a rate of 3kr/s for 30s, the thickness was measured to be 1 μm.

Phosphorus ions were implanted into PMMA-coated MoS_2 samples by a Varian CF3000 implanter in the Hong Kong University of Science and Technology. The implantation energy was 10 keV and the implantation dose was 5×10^{13} cm^{-2}.

A LabRAM HR 800 Raman Spectrometer was used to collect Raman and PL spectra of MoS_2 samples. The wavelength of light source is 488 nm and the power density is 50 mW.

Conventional photo-lithography process is performed by a SUSS MA6 Aligner, followed by metal deposition and lift-off process. Metal electrodes (*i.e.*, 5 nm Ti/ 50 nm Au) are deposited by electron-beam evaporator at a rate of ~0.7 Å s^{-1} in ultra-high vacuum. Electrical characteristics of the FETs were measured by a Lakeshore Low Temperature IV Probe Station.

2.4 Results and Discussion of PMMA-assisted Ion-Implantation of MoS_2

2.4.1 Characterizations of MoS_2 Lattice after Implantation

Ultrathin MoS_2 flakes are mechanically exfoliated by Scotch tape onto 300 nm SiO_2/Si substrates and identified under microscope (**Figure 2.3**a). The

thickness of MoS_2 is identified by the contrast on the SiO_2 substrate. 1-4L MoS_2 are implanted under the same conditions. PMMA is spin-coated onto the samples at various spin speed and hardened by post-baking at 180 °C for 1min. Two different thickness of PMMA layers are applied in this experiment, 200-nm-thickness and 1-μm-thickness. With the protection of PMMA layer, MoS_2 flakes were implanted by phosphorus ions with implantation energy varying from 10 keV to 40 keV and the dose of 5×10^{13} cm^{-2} (Figure 2.3(b)). After the implantation, PMMA layer is then removed by bathing in Acetone and IPA. For TEM characterizations, implanted samples are wet-transferred to copper grids. The TEM and HRTEM pictures are shown in Figure 2.3(c)-(d). The wrinkles on the MoS_2 flakes are probably introduced during the transferring process. The electron diffraction pattern shows that the implanted MoS_2 samples are well-crystallized. HRTEM also shows highly ordered hexagonal lattice structure of implanted MoS_2 samples. It is noteworthy that due to its Z^2 contrast dependency, we can only identify Molybdenum atoms in HRTEM image.[24] Substitutions or vacancies of sulfur atoms cannot be identified.

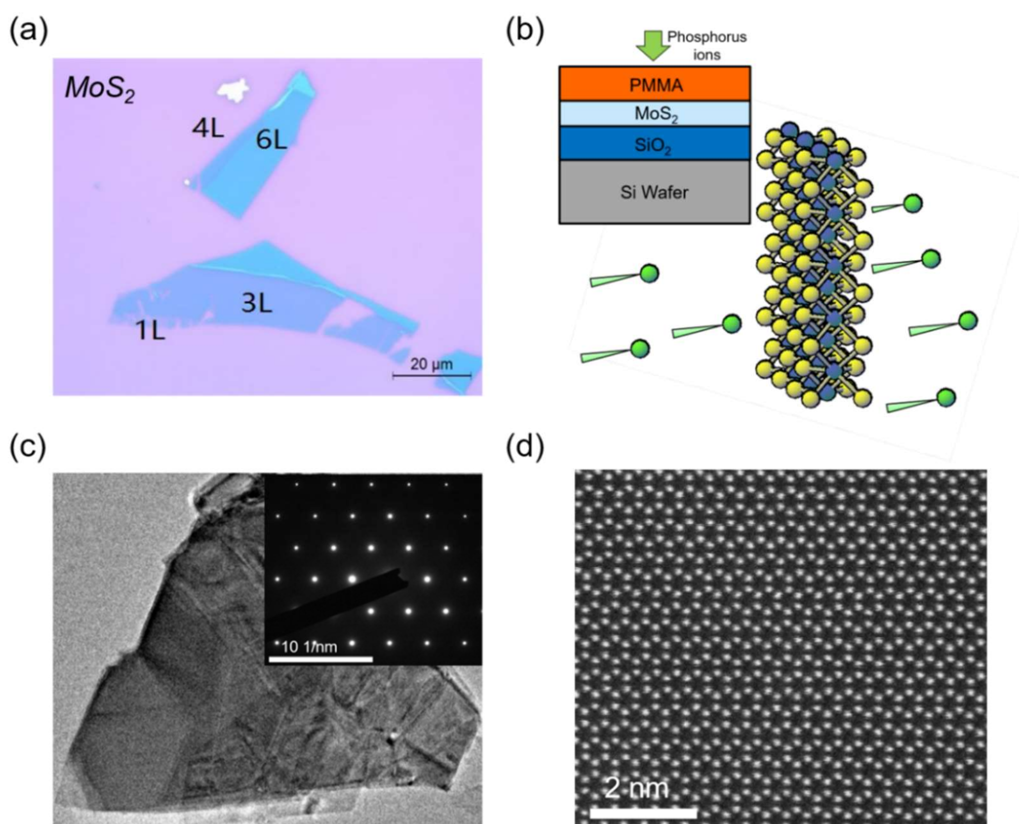

Figure 2.3 Schematic of PMMA-assisted ion-implantation and TEM characterizations. (a) Microscope image of MoS_2 thin flakes exfoliated onto 300 nm thick SiO_2/Si substrate. (b) Cross-sectional schematic of PMMA-assisted ion-implantation process. (c) TEM image of the MoS_2 flake after ion-implantation. The inset shows the electron diffraction pattern. (d) HRTEM image of the MoS_2 flake after ion-implantation.

Raman is a non-destructive and statistical characterization method of crystal lattice. Different from TEM or HRTEM characterizations, Raman spectra can reveal the change of sulfur atom sites as well as molybdenum atom sites. Raman spectra shows the statistical results of MoS_2 in a square area of ~ 1 μm^2. Two Raman peaks of MoS_2, namely E_{2g}^1 (~380 cm^{-1}) and A_{1g} (~400 cm^{-1}), are analyzed

in our experiments. E_{2g}^1 is sensitive to in-plane vibrations while A_{1g} is sensitive to out-of-plane vibrations (**Figure 2.4**(a)).[57-59] The frequency of Raman peaks reveals the lattice symmetry and lattice parameters. While the Full Width Half Maximum (FWHM) of Raman peaks shows the crystallization of MoS_2 samples. The FWHM is smaller for better crystallization and *vice versa*. Raman spectra of ultrathin MoS_2 flakes were collected both before and after ion-implantation. Figure 2.4(a) shows the Raman spectra of 2L MoS_2 before and after implantation under the protection of 200-nm-thick PMMA. The Raman spectra are normalized by the intensity of E_{2g}^1 peak. After the implantation, E_{2g}^1 peak is blue shifted for about 1 cm^{-1} and A_{1g} peak is blue shifted for about 2 cm^{-1} and the FWHM of A_{1g} peak is increased for about 2 cm^{-1} (the measurement accuracy of the Raman system used is 0.6 cm^{-1}). Figure 2.4(b) shows the Raman spectra of 4L MoS_2 flake before and after implantation under the protection of 200-nm-thick PMMA as well. There is only negligible change of the Raman peaks and the Raman spectra before and after implantation almost coincide. This result shows that 4L MoS_2 endures smaller lattice damage during the implantation process than 2L MoS_2. Figure 2.4(c) shows the Raman spectra of 2L MoS_2 before and after implantation under the protection of 1-μm-thick PMMA. There is no change of the E_{2g}^1 peak while the A_{1g} peak has been blue-shifted and broadened. Figure 2.4(d) shows the Raman spectra of 4L MoS_2 before and after implantation under the protection of 1-μm-thick PMMA. Only small blue-shift has been observed for the A_{1g} peak after implantation. It is obvious that under the same implantation conditions, 4L MoS_2 has much smaller change of Raman spectra than 2L MoS_2. To reveal the relationship of Raman

change and MoS_2 thickness or PMMA thickness, the frequency and full-width-at-half-maximum (FWHM) of E_{2g}^1 and A_{1g} of all implanted samples are summarized in Figure 2.4(e)-(f). It is demonstrated that for thicker MoS_2, the change of Raman spectra is smaller than thinner MoS_2 under the same conditions. Thicker PMMA leads to relatively smaller change of MoS_2 Raman than thinner PMMA layer under the same conditions. It is straightforward that thicker PMMA protects beneath MoS_2 from bombarding ions better. It is suggested that the major of implanted ions is stopped within the top few layers of MoS_2 while the underlying layers remain intact. This observation is consistent with previous reports.[24,25,32]

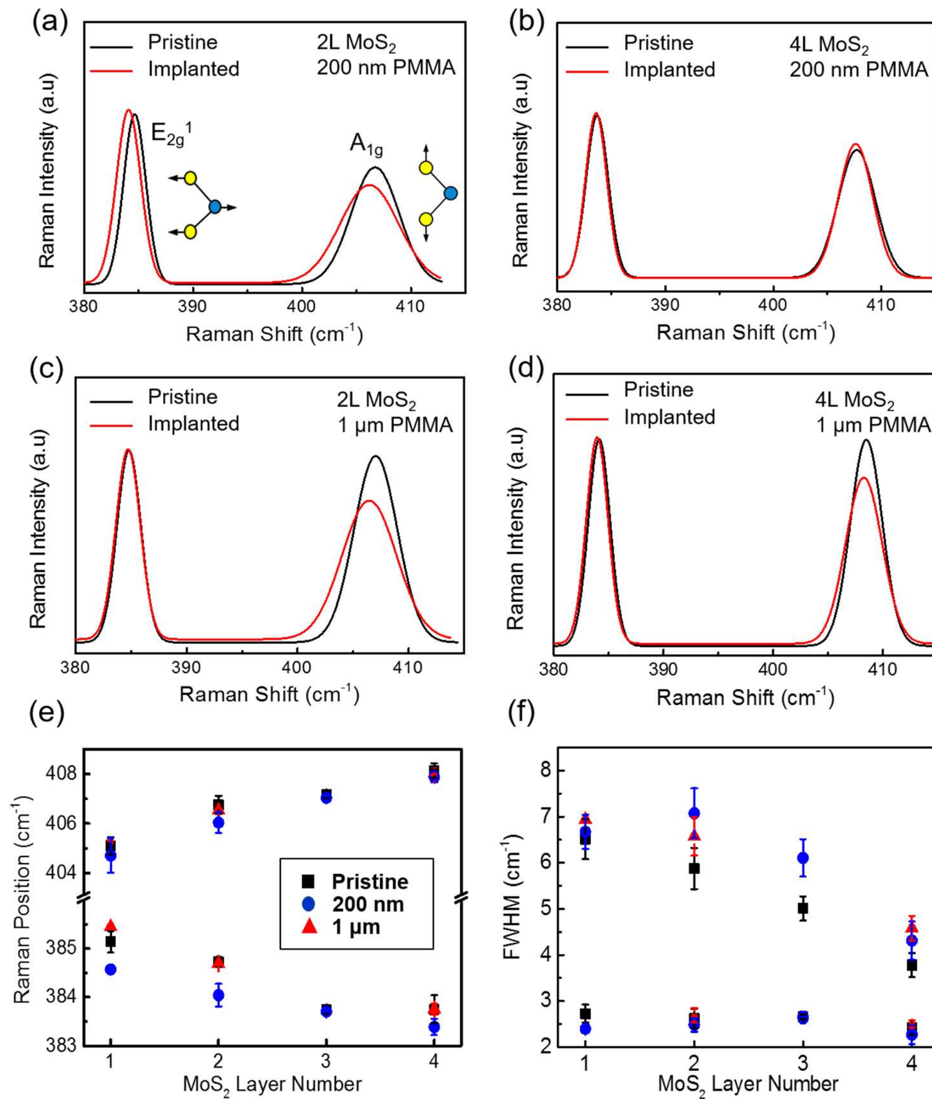

Figure 2.4 Raman characterizations of MoS_2 after ion-implantation. (a)-(d) Normalized Raman spectra of 2L and 4L MoS_2 before and after ion-implantation. The results of both 200-nm-thick PMMA protection (a)-(b) and 1-μm-thick PMMA protection are presented. (e) Summary of the position of MoS_2 Raman peaks before (black) and after ion-implantation, under the protection of 200-nm-thick (blue) and 1-μm-thick PMMA (red). (f) Summary of the FWHM of MoS_2 Raman peaks before (black) and after ion-implantation, under the protection of 200-nm-thick (blue) and 1-μm-thick PMMA (red).

2.4.2 Characterizations of Doping Effect

An exciton is composed of an electron and a hole. The electron and hole in an exciton is bonded by electrostatic interaction. Thus, an exciton is neutrally charged. A trion is composed by an exciton and an electron or a hole. Thus, a trion is negatively charged or positively charged. In traditional bulk materials, excitons or trions cannot exist stably at room temperature. Because the boding energy of exciton or trion is too small, so they are easy to be decomposed by thermal disturbtion. However, due to strong Columb screening effect, photo-generated and tightly bond excitons and trions can exist in ultrathin MoS_2 at room temperature.[10,16,59] So, they can be detected and analyzed by PL measurement. Trions are formed in the presence of residual free charges. [60] Exfoliated MoS_2 flakes are n-doped by surface sulfur vacancies, so there are extra free electrons in the body of MoS_2. Because it is energy-favorable for excitons to be bonded with free electrons, trions in MoS_2 are negatively charged.[10,16] The typical PL spectrum of MoS_2 is composed of the indirect bandgap peak, negative trion X^-, neutral exciton X and B exciton (**Figure 2.5**(a)). The negative trion X^- peak and the neutral exciton X peak are measured and analyzed in this study. The spectral weight of the X^- peak is positively proportional to the free electron density in MoS_2, so it is an indication of the doping effect in MoS_2.[61] For example, the spectral weight of X^- peak is expected to increase if the MoS_2 sample is n-doped and the spectral weight of X- peak is expected to decrease if the MoS_2 sample is p-doped.

The doping effects of MoS_2 samples implanted at an acceleration energy of 10 keV are analyzed and discussed in this part. By the Stopping and Range of Ions

in Matter (SRIM) simulation, the approximated stopping range of phosphorus ions in PMMA accelerated at 10 keV is smaller than the thickness of PMMA (200 nm) adopted in our experiments. This discrepancy might originate from the difference between the ideal case in theoretical model and the practical situation of PMMA in our experiments. The effective density of PMMA in our experiment could be lower than that in ideal case, which can give rise to relative larger transverse depth than theoretical simulation. Ultrathin MoS_2 flakes are easy to react with moisture and oxygen at high temperature. To protect MoS_2 flakes, the substrates with MoS_2 were not pre-baked nor cleaned by O_2 plasma before spin-coating PMMA, which is typically required in the standard process. As a result, some moisture and gas molecules are inevitably adhesive on the surface of silicon substrates in this case. In addition, the PMMA was baked at the temperature of 180 °C for 1 min, which is a relative short time compared with the baking time (3 min, 5 min, 20min, 30 - 90 min) adopted in many other reports. [29-33] As a result, the solvents in the PMMA were not completely removed in our work. When we load the sample into vacuum chamber for ion implantation, the outgassing of the samples in the vacuum chamber will happen and create porosity inside PMMA, which results in an increased stopping range for the phosphorus ions.

In this study, we observe that the change of the spectral weight of the negative trion X^- peak after the implantation is dependent on both the thickness of MoS_2 sample and the thickness of PMMA used during the implantation process. Figure 2.5(b) shows the PL spectra of 2L MoS_2 before and after implantation under the protection of 200-nm-thick PMMA. After the implantation, the spectral weight of

the negative trion X^- peak is dramatically increased. This result indicates that 2L MoS_2 is n-doped. Due to the ultrathin nature of 2L MoS_2, implanted phosphorus ions penetrate the lattice of MoS_2 and create sulfur vacancies. Sulfur vacancies have n-doping effect on MoS_2. Figure 2.5(c) shows the PL spectra of 4L MoS_2 before and after implantation under the protection of 200-nm-thick PMMA. The negative trion X^- peak is dramatically decreased after implantation. It demonstrates that phosphorus ions are retained inside MoS_2 and have p-doping effect on MoS_2. Figure 2.5(d) shows the PL spectra of 2L MoS_2 before and after implantation under the protection of 1-μm-thick PMMA. There is almost no change of the spectral weight of the negative trion X- peak after implantation. Comparing with Figure 2.5(b), it shows that increasing the thickness of PMMA effetely reduces the damage to MoS_2 lattice during the implantation process. Figure 2.5(e) shows the PL spectra of 4L MoS_2 before and after the implantation under the protection of 1-μm-thick PMMA. There is negligible change of the spectral weight of the negative trion X^- peak. Comparing with Figure 2.5(c). it shows that increasing the thickness of PMMA also decreases the p-doping effect on relative thick MoS_2 samples. The spectral weight of the negative trion X^- peak of all implanted samples are summarized in Figure 2.5(f). Two conclusions can be drawn from Figure 2.5(f). First, the doping effect with 200-nm-thick PMMA has much stronger layer dependence than 1-μm-thick PMMA. Under the protection of 200-nm-thick PMMA, MoS_2 samples thinner than 3L are highly n-doped; while MoS_2 samples thicker than 3L are highly p-doped. On the other hand, under the protection of 1-μm-thick PMMA, both of 2L and 4L MoS_2 samples are slightly p-doped. But under

the same implantation conditions, 1-μm-thick PMMA leads to decreased p-doping effect than 200-nm-thick PMMA. Second, the implantation process has less damage to the structure of thicker MoS_2 and much more p-doping effect to thicker MoS_2. It is easy to understand these conclusions since both the layer of PMMA and the top few layers of MoS_2 act as sacrificial layers to decelerate impacting phosphorus ions. To sum up, the thickness of PMMA is negatively proportional to the p-doping effect while the thickness of MoS_2 is positively proportional to the p-doping effect. By selecting appropriate thickness of MoS_2 and PMMA, the doping effect can be tuned in a controllable manner.

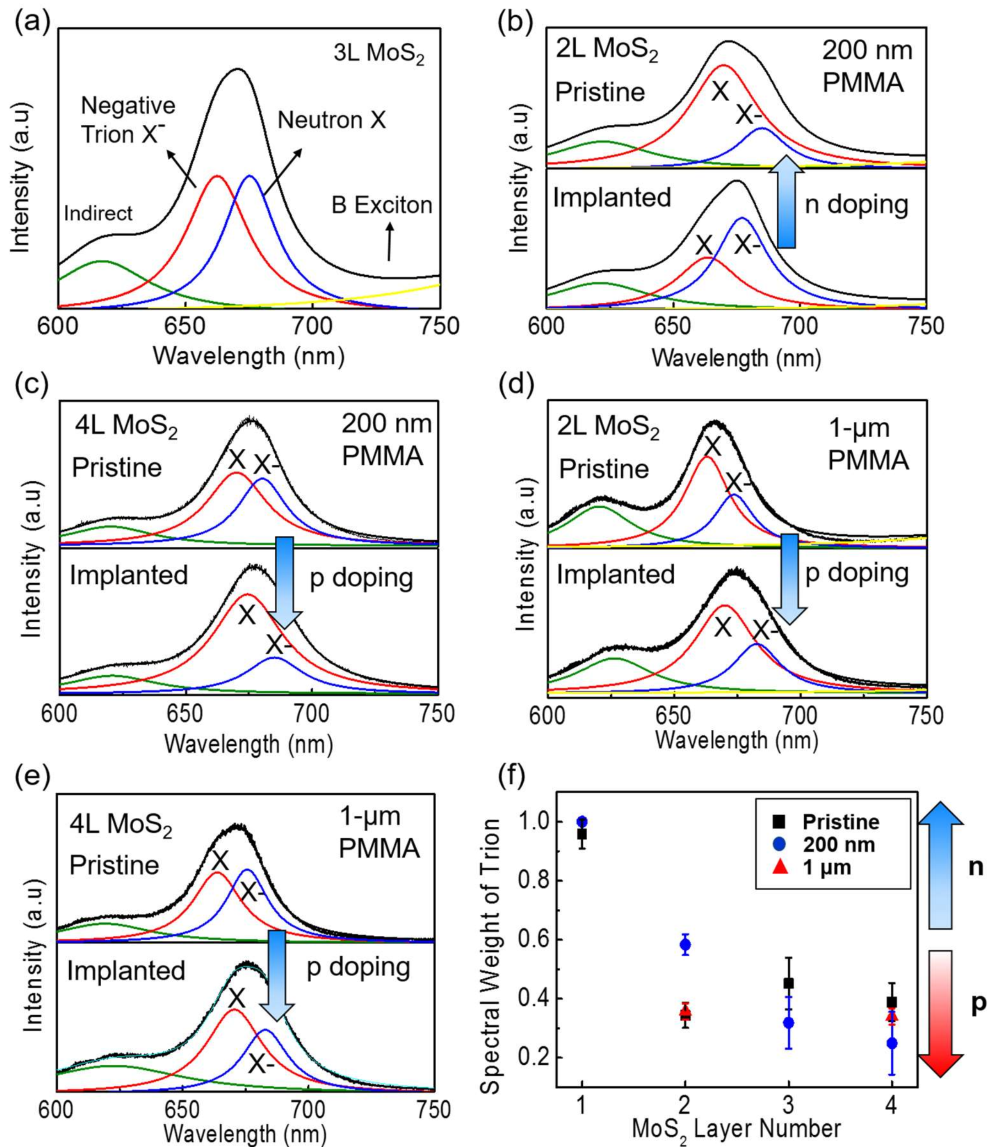

Figure 2.5 PL characterizations of MoS_2 after ion-implantation. (a) Decomposition of PL spectra of 3L MoS2. (a)-(d) PL spectra of 2L and 4L MoS_2 before and after phosphorus implantation. MoS_2 samples are implanted under the protection of 200-nm-thick PMMA and 1-μm-thick PMMA, respectively. (f) PL spectra summary of implanted MoS_2 samples. Black, blue and red dots represent pristine samples, samples implanted underneath 200-nm-thick PMMA and samples implanted underneath 1-μm-thick PMMA, respectively.

To demonstrate this doping strategy more straightforwardly, few layer MoS_2 field effect transistors are fabricated and then implanted by the same implantation process as described above. Based on the optical characterization results, the thickness of MoS_2 is chosen to be 5L and the thickness of PMMA is chosen to be 200 nm so that the best p-doping effect can be expected. **Figure 2.6**(a) illustrates the cross-sectional schematic of few-layer MoS_2 FET. Since the device is implanted after fabrication, the body of MoS_2 under the metal contacts are not implanted with phosphorus ions. So, the regions under the contacts are n-type. Only the channel is implanted with phosphorus ions. Figure 2.6(b) shows the transfer curve of this device before and after implantation. The inset shows the optical image of the FET as fabricated. This device shows obvious n-type characteristic both before and after implantation due to the intrinsic sulfur vacancies. After the implantation, the ON-current in the range of positive gate voltage is obviously decreased for about 5 times. Also, the threshold voltage is increased from -45 V before implantation to -20 V after the implantation. Because there are less free electrons in MoS_2, the electron density contribute to the current is smaller at the same gate voltage and a larger gate voltage is required to turn on the channel. We do not observe p-type transport in our experiments. Because the regions under the contacts are not p-doped and shows n-type transport characteristics. Due to the ultrathin nature of our MoS_2 device, the contacts play an important role in its electrical transportation. The n-type transport characteristic of the contacts significantly suppresses the p-type transport characteristic in the channel material. The output curves of this device before and after doping are

presented in Figure 2.6(c) and Figure 2.6(d), respectively. The ON-current is found to be decreased for about 4 times at the same gate voltage. The gate voltage required to turn on the channel is increased form -10 V to 10 V. Furthermore, it is worth to note that p-type transport in MoS_2 FET can be realized by this doping method. Few-layer MoS_2 samples can be implanted first and then transferred to a fresh new substrate. Then the FET is fabricated upon the p-doped MoS_2.

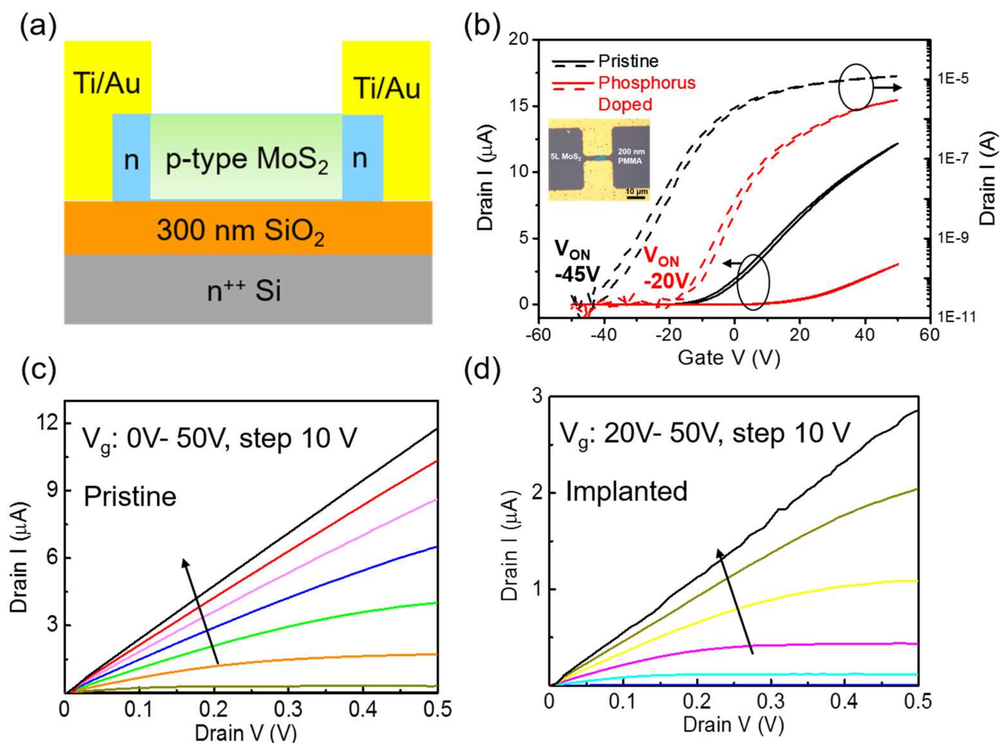

Figure 2.6 Electrical characterizations of MoS_2 sFET. (a) Cross-sectional schematic of MoS_2 FET after ion-implantation. (b) Transfer curve of a 5L MoS_2 FET before (black line) and after (red line) implantation. The inset shows the optical image of this device. (c) Output curves of the device before implantation. (d) Output curves of the device after implantation.

2.4.3 Implantation-Energy-Dependent Doping Effect

MoS_2 flakes with similar thickness (~ 4L) have been implanted at various implantation energies, namely 10 keV, 20 keV, 30 keV and 40 keV. The doping effects are characterized and analyzed by PL spectra (**Figure 2.7**). Figure 2.7(a)–(c) show the PL spectra of MoS_2 flakes implanted by high implantation energy. There is less decrease in the spectral weight of negative trion peak as a function of implantation energy, indicating a decreased p-doping effect with the increase of implantation energy. As summarized in Figure 2.7(d), the decrease of negative trion spectral weight at 40 keV is about 12.5% of that at 10 keV. This indicates that the p-doping effect at 40 keV is about 12.5% of that at 10 keV. Since the spectral weight of negative trion peak is positively proportional to the electron density in MoS_2, less decrease in the spectral weight of negative trion peak suggests less p-doping effect. With increased implantation energy, dopants are implanted into MoS_2 lattice at higher velocity, which creates more defects. Sulfur vacancies lead to n-doping effect of MoS_2. The PL spectra show the trade-off between the p-doping effect and creation of defect sites. Among the implantation energies, 10 keV is found to achieve the best p-doping effect by maximizing the incorporation of p^+ into MoS_2 lattice while minimizing the knock-off effect to atomic sites in MoS_2.

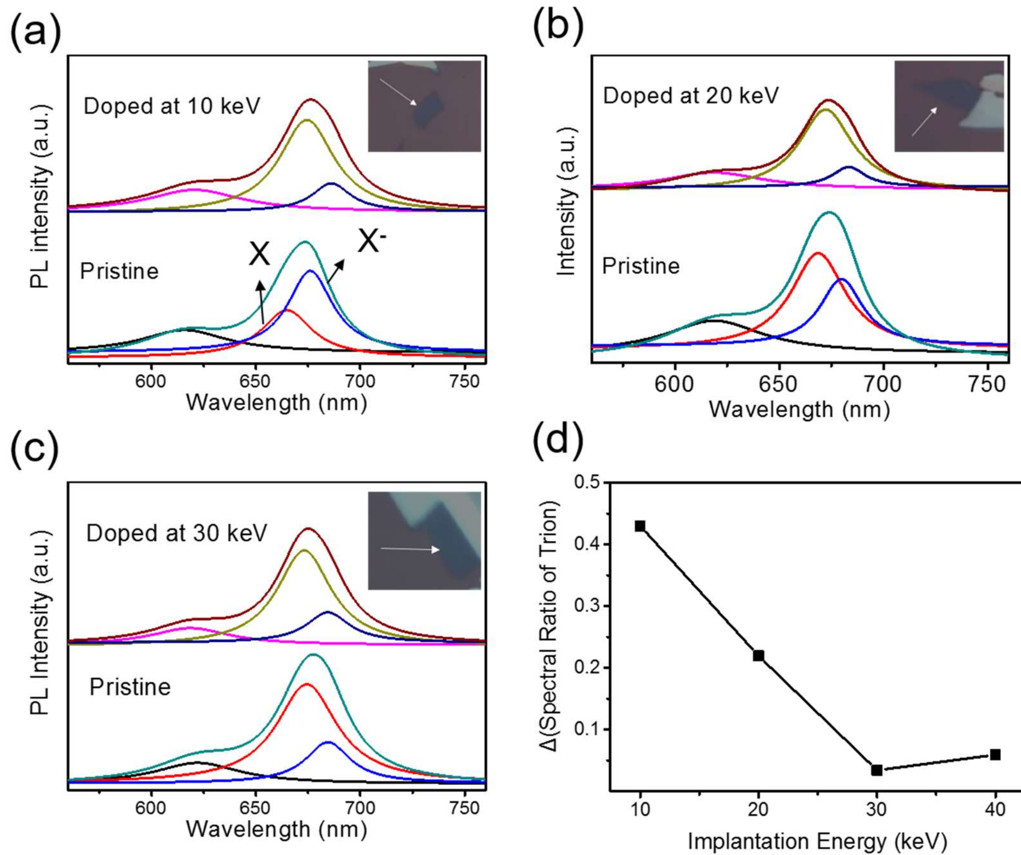

Figure 2.7. Implantation energy dependent doping effect. The PL spectra comparison between pristine and doped samples at the implantation energy of (a) 10 keV, (b) 20 keV and (c) 30 keV. (d) Summary of the decrease of trion spectral weight after implantation at different implantation energies.

2.5 Summary

The doping of 2D MoS_2 by traditional ion-implanters has been exploited. HRTEM and electron diffraction pattern reveal that the crystal structure of 2D MoS_2 remained well after implantation. By analyzing Raman spectra of MoS_2, it is suggested that the major of implanted ions are deaccelerated by the top few layers of MoS_2, while the underlying layers are less affected. PL spectra of ultrathin MoS_2 show significant p-doping effect in relative thick samples (> 3L).

The p-doping effect is also demonstrated by FET characterizations. We found that the damage caused by high-energy dopant ions to MoS_2 can be significantly reduced by spin-coating a protection layer of PMMA on top of MoS_2 as a protection layer. The dopant depth can be adjusted by varying the thickness of PMMA. Thinner PMMA leads to larger kinetic damage but also more significant doing effect. Also, the kinetic damage could be effectively reduced by increasing the thickness of MoS_2. With increased implanting energy (from 10 keV to 40 keV), the stopping range of implanted phosphorus ions are increased, so more ions are incorporated into MoS_2 flakes at higher velocities. Thus, the damage to MoS_2 lattice is increased, which induces more sulfur vacancies and leads to a decreased p-doping effect. More detailed characterizations of this doping strategy are required.

Chapter 3: Modulation Doping of Transition Metal Dichalocogenides/Oxides Heterostructure

3.1 Introduction

Various methods have been developed to dope 2D layered materials, including substitutional doping during growth, [10] ion implantation, [11] plasma treating, [12] *etc*. Although these doping methods have been demonstrated to be effective in modifying the carrier type and carrier density in 2D semiconductors, they inevitably result in the distortion or damage of the crystal structure of 2D materials, introduce ionized impurity scattering center, and degrade the charge mobility. Degraded charge mobility leads to degraded performance of 2D devices. On the other hand, modulation doping has been widely used in III-V compound heterojunction superlattices to eliminate the influence of the ionized impurity scattering. [13-15] In the heterojunction device, the ionized dopants and electrons are confined into two different adjacent layers. Free electrons are transferred between the dopant layer and the target material. Transporting electrons in the target material are not scattered by the ionized ions in the dopant material. As a result, the mobility and carrier concentration are both well maintained. A variety of dopants have been studied for the surface charge transfer to 2D materials, including gas molecules, [16] organics, [17] metal particles [18] and oxides. [2, 19] Among these kinds of dopants, oxide is one promising specie due to its stability in

ambient and compatibility with conventional Si processing technology.

In this work, we deposit transition metal oxide (TMO) on top of 2D MoS_2 to form a heterojunction device. We choose TiO_2 with high charge neutrality level (CNL) for injecting electrons into MoS_2 and MoO_3 with low CNL for extracting electrons from MoS_2. Our optical and electrical characterizations, together with density functional theory (DFT) calculations, show that TiO_2 and MoO_3 deposition give rise to effective n-, and p-doping, respectively. This approach opens up a way to control the characteristics of PL and electrical transport of 2D layered materials.

3.2 Experimental Preparations

MoS_2 crystals were purchased from commercial producer (2D Semiconductors). Mechanically exfoliated MoS_2 thin flakes were used to fabricate FETs. Target substrates (300-nm-thick SiO_2/Si wafer) were contacted with Scotch tape and then bathed in Acetone or Isopropyl Alcohol (IPA) at 60 °C to remove organic residues. Ultrathin flakes (< 10 nm) of MoS_2 were identified under optical microscope. Conventional photo-lithography process was performed, followed by metal deposition and lift-off process. Metal electrodes (*i.e.* 5 nm/50 nm Ti/Au) were deposited by electron-beam evaporator at a rate of ~0.7 Å s^{-1}. Electrical characteristics of the FETs were measured by a Keithley 4200-SCS Semiconductor Parameter Analyzer.

TiO_2 oxide layers were deposited on MoS_2 FETs by ALD at 150 °C. The sources were tetrakis(dimethylamino)titanium (TDMAT) and H_2O. The deposition rate was ~0.47 Å $cycle^{-1}$. Thermal evaporator was used to deposit MoO_3 oxide layers. The source was MoO_3 powder. The deposition rate was around 1 Å s^{-1}. The

oxide layers are continuous and have small surface roughness.

A LabRAM HR 800 Raman Spectrometer was used to collect Raman and PL spectra of MoS_2 flakes. A 488 nm laser was focused on the selected samples by 100× microscope lens and used as the excitation source.

The DFT calculation were conducted by Quantum ESPRESSO to deduce the charge transfer between oxide and TMDs. The projector-augmented wave sets, scalar relativistic pseudopotentials were used to describe the ion cores. The generalized gradient approximation Perdew–Burke–Ernzerhof (PBE) exchange-correlation was selected as the pseudopotential functional type. 2×1×1 monolayer MoO_3 was constituted on the top of 2×1×1 1H-MoS_2 along the (001) direction; 2×1×1 TiO_2 was constituted on the 2×1×1 1H-MoS_2 along the (001) direction. Each supercell contains a 40 Å vacuum region in z-axis to prevent the effects from neighbor slabs. The convergence threshold on total energy and force were 10^{-6} and 10^{-3}, respectively. The kinetic energy cutoff for wave functions was 50 Ry, and the kinetic energy cutoff for charge density and potential was 200 Ry.

3.3 Results and Discussion

3.3.1 Layer-dependent Negative Trion PL of 2D MoS_2

Because of the extremely strong Coulomb interaction in ultrathin 2D MoS_2, optically generated excitons (i.e., electron-hole pairs) and trions (i.e., charged excitons) can exist stably at room temperature.[16] Electrons are excited to the conducting band, leaving holes in the valence band. Electrons and holes are then bound together by Columb interaction to form neutrally charged excitons

(electron-hole pair). Due to the Columb attraction between the hole in an exciton and a third electron, the formation process of exciton to trion is energy favourable.[62] Trions are formed in the presence of residual free charges. **Figure 3.1**(a) shows the PL spectra of an 3L MoS_2 as an example. Two pronounced peaks around 1.87 eV and 2.05 eV are clearly observed, defined as the A exciton peak and the B exciton peak, respectively. As schematically depicted in the inset, the A exciton is originated from the radiative recombination of the excited electrons in the conduction band minimum (CBM) with the holes in the valance band minimum (VBM); and the B exciton is originated from the radiative recombination of the excited electrons in the CBM with the lower branch of split VBM.[60] The A exciton of ultrathin MoS_2 can be further devolved into a neutron exciton (X) peak around 1.9 eV and a negative trion (X^-) peak around 1.85 eV.[16]

Figure 3.1(b) shows the PL spectra of MoS_2 evolved with the layer number from 1L to 4L. Because as the thickness of MoS_2 increases, the bandgap of MoS_2 decreases, so the PL peaks of MoS_2 red-shift. PL spectra of over 60 MoS_2 flakes were collected and summarized in Figure 3.1(c) and Figure 3.1(d). Figure 3.1(c) shows the layer-dependent spectral weight of the negative trion X^- peak in the whole A exciton peak. The spectral weight of X^- peak rapidly decreases from 90% in the 1L MoS_2 to 30% in the 3-5L MoS_2. There are two possible reasons accounting for this layer-dependent characteristic of the spectral weight of X^- peak. First, there are sulfur vacancies in MoS_2, and these vacancies introduce donor states near the conduction band of MoS_2. Extra free electrons in MoS_2 are originated from these donor states introduced by surface sulfur vacancies.[42,63,64]

When the thickness of MoS_2 increases, the influence of surface sulfur vacancies decreases, so the concentration of extra free electrons decreases. So, the spectral weight of negative trion peak decreases as well. Second, when the thickness of MoS_2 increases, the dielectric screening of MoS_2 increases.[65,66] The increased dielectric screening attenuates the Columb interaction and reduces the binding energy of trions.[10] With the decrease of binding energy, trion systems are less stable and can be easily decomposed into excitons by thermal disturbtion. Figure 3.1(d) shows the photon energy of X and X^- peak versus the thickness of MoS_2. The PL peaks exhibit clear red-shift with the increase of MoS_2 body thickness due to decreased bandgap. In the inset of Figure 3.1(d), we present the layer-dependent energy difference (binding energy of negative trion from exciton) between X and X^- peak. When the thickness of MoS_2 increases, the energy difference between the neutron exciton and negative trion decreases and so it is less energy favorable for excitons to form trions.

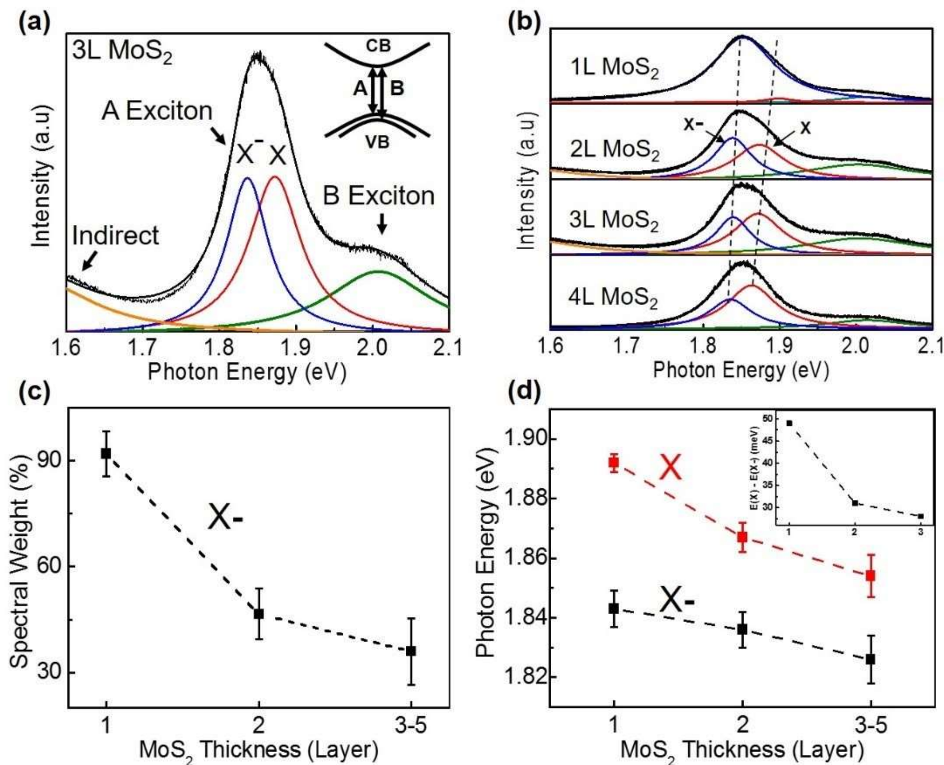

Figure 3.1 Layer-dependent PL analysis of ultrathin MoS_2 flakes. (a) PL spectrum of an 3L MoS_2. The inset shows the radiative recombination path of A and B exciton, respectively. (b) PL spectra of 1-4L MoS_2. (c) Layer-dependent spectral weight of X^- peak. (d) Layer-dependent photon energy of X peak and X^- peak in the MoS_2 samples, from 1L to 5L. The inset shows the layer-dependent energy difference between X peak and X^- peak.

3.2.2 Layer-dependent n-doping of MoS_2 by Surface Charge Transfer from TiO_2

Figure 3.2 shows the PL spectra of 1L-4L MoS_2 before and after 6-nm-thick TiO_2 deposition. Figure 3.2(a) shows the PL spectra of 1L MoS_2 before and after doping. The spectral weight of negative trion peak is slightly decreased. This means that 1L MoS_2 is slightly p-doped by TiO_2. Figure 3.2(b) shows the PL spectra of 2L MoS_2 before and after doping. There is negligible change of the

spectral weight of the negative trion. It indicates that TiO_2 has no doping effect on 2L MoS_2. Figure 3.2(c) shows the PL spectra of 3L MoS_2 before and after doping. The spectral weight of negative trion peak is slightly increased. This indicates that 3L MoS_2 is slightly n-doped by TiO_2. Figure 3.2(d) shows the PL spectra of 4L MoS_2 before and after doping. We see an obvious increase of the spectral weight of negative trion peak. This demonstrates that TiO_2 has a strong n-doping effect on 4L MoS_2.To sum up, after 6-nm-thick Atomic Layer Deposition (ALD) TiO_2 doping, we observe a characteristic of layer-dependent change of MoS_2 PL. Thicker MoS_2 sample has smaller X^- spectral weight before the TiO_2 deposition, which is consistent with our previous discussions; while the X^- spectral weight increases more after the TiO_2 deposition than thinner MoS_2 samples. These changes of PL spectra are originated from the layer-dependent band-structure nature of MoS_2.

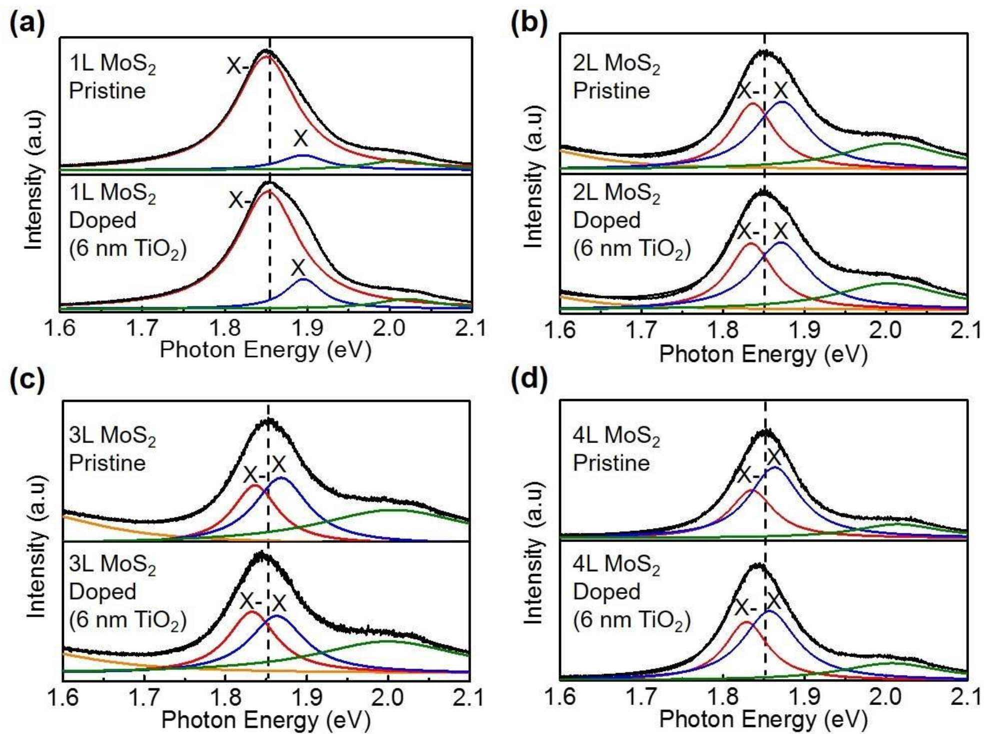

Figure 3.2 PL spectra of ultrathin MoS_2 flakes before and after depositing 6-nm-thick TiO_2. The thickness of MoS_2 samples are (a) 1L, (b) 2L, (c) 3L and (d) 4L.

To rule out the possibility that this PL change is originated from in-plane lattice strain due to the deposition of oxide layer on the surface, we also present corresponding Raman spectra before and after doping in **Figure 3.3**. Because Raman is a non-destructive and statistical characterization method of crystal lattice structure. As widely reported by previous researches, in-plane lattice strain results in the split of E_{2g}^1 peak and blue-shift of both E_{2g}^1 and A_{1g} peaks.[67] However, from our Raman spectra, we observe no such Raman spectra change. Thus, it is suggested that the interface coupling between TiO_2 layer and MoS_2 surface is weak van der Waals interaction and this weak interaction induces negligible lattice strain

to MoS_2. So, the PL spectra change is not originated from lattice strain.

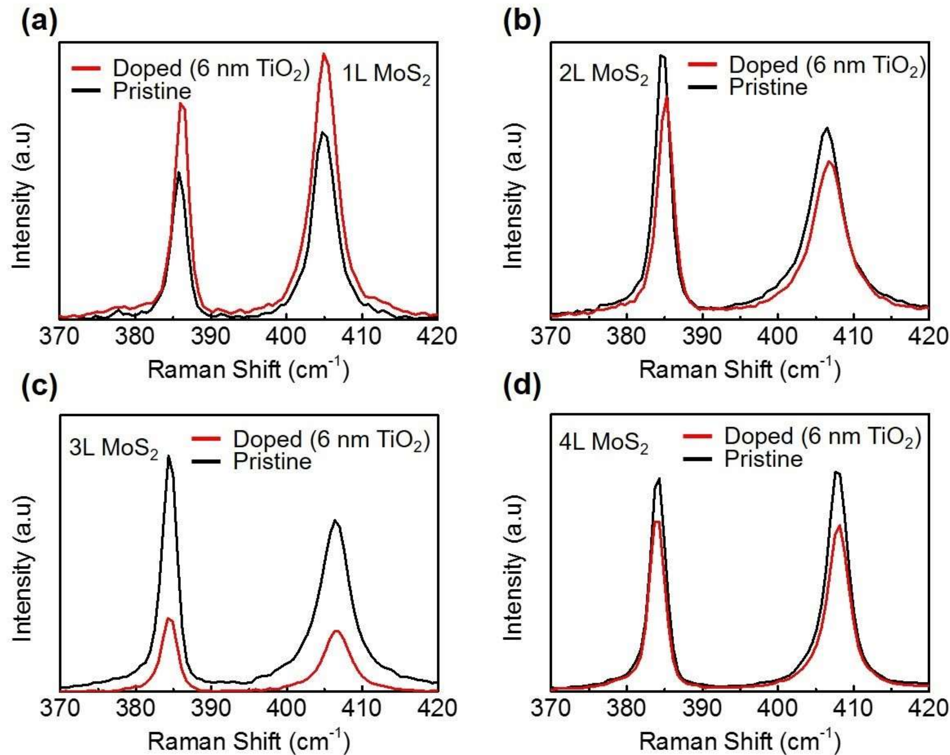

Figure 3.3 Raman spectra of 1-4L MoS_2 before (black line) and after (red line) 6-nm-thick TiO_2 doping.

To further demonstrate this conclusion, we further deposited 1-3L MoS_2 by 30-nm-thick TiO_2. The Raman and PL spectra of MoS_2 before and after doping are shown in **Figure 3.4**. Again, we observe more significant increase of X^- spectral weight in thicker MoS_2 than in thinner MoS_2 and we also observe only negligible shift of Raman peaks. It is noteworthy that the attenuation of Raman intensity after the doping is possibly because part of the light is blocked by the oxide layer deposited on the surface of MoS_2. On the other hand, as a high-k material, the deposition of TiO_2 leads to significant change of the dielectric environment for

MoS_2. The change of the dielectric environment has significant influence over the PL spectra of MoS_2 as well. In both cases (6-nm-thick and 30-nm-thick TiO_2), the A exciton peak is found to be red-shifted after the TiO_2 deposition. This change is more obvious in the case of 30-nm-thick TiO_2 deposition, which leads to much stronger change of the dielectric environment. This is because the bandgap of MoS_2 is decreased under the environment with higher dielectric constant (dielectric constant of TiO_2 ~ 80).[10] Further, due to the deposition of oxide layer, the dielectric screening in MoS_2 is increased, and the Columb interaction in MoS_2 is attenuated (similar to the effect of increasing MoS_2 body thickness). The attenuated Columb interaction decreases the binding energy of negative trion and leads to smaller energy difference between neutral excitons and negative trions. So, it is less energy favorable for excitons to be formed into trions. Thus, the spectral weight of negative trion peak should be decreased after the deposition of TiO_2 as a result. However, in our experiments, the spectral weight of the negative trion peak is obviously increased after the TiO_2 doping. Therefore, the increase of X^- peak PL is due to the increase of electron density in MoS_2, originated from the n-doing effect by TiO_2.

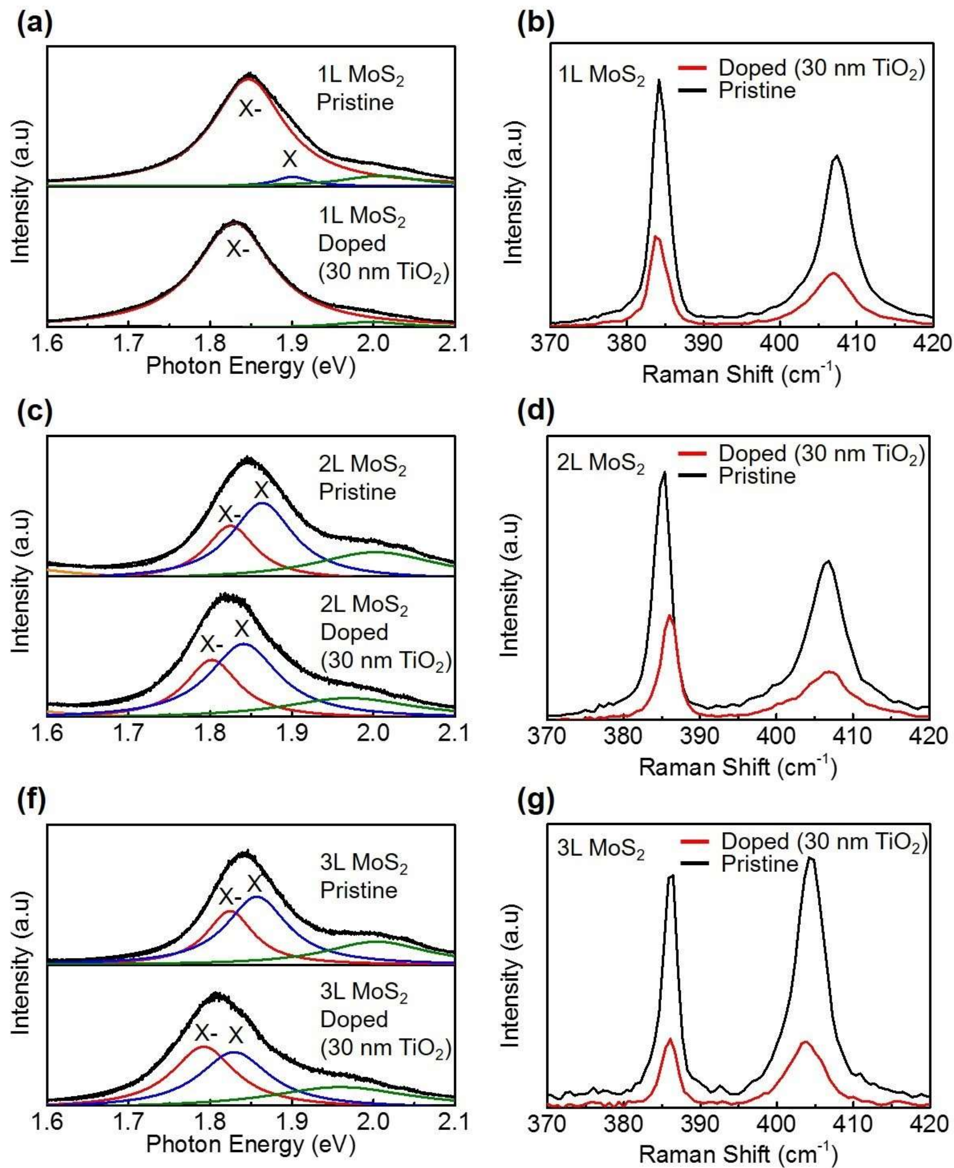

Figure 3.4 PL and Raman spectra of 1L-3L MoS_2 before and after being doped with 30-nm-thick TiO_2. The three panels listed on the left side are PL spectra and those listed on the right side are corresponding Raman spectra.

To demonstrate the n-doping effect of TiO_2 more straightforwardly and to quantify the n-doping effect. We fabricated back-gated few-layer MoS_2 field effect transistor (FET) and doped it with 6-nm-thick ALD TiO_2. **Figure 3.5**(a) depicts

the cross-sectional schematic of a back-gated MoS_2 FET with its channel covered by TMO. There is only weak van der Waals interaction between MoS_2 and TMO. Fig. 5.5(b) shows the transfer curve of a 5L MoS_2 FET before (black line) and after (red line) the 6-nm-thick TiO_2 doping. The pristine device shows typical n-type behavior, in consistent with previous reports.[1,68] After n-doping, the ON Current (I_{ON}) is increased by a factor of 4 at V_{bg} = 50 V. Figure 3.5(c) and Figure 3.5(d) show the output curves of the same device before and after doping, respectively. Again, I_{ON} at V_{bg} = 50 V is found to be amplified by about 5 times. It is noteworthy that the device remains its semiconducting characteristic after the doping, indicating that the n-doping effect is non-degenerate. Further, we can extract 2D sheet carrier density (n_{2D}) and field-effect mobility (μ_{FE}) according to Equation 5.1, in which L and W are the channel length and the channel width, respectively, C_{ox} is the capacitance of gate oxide, (*i.e.*, 1.16×10^{-8} F/cm^2 for 300-nm-thick SiO_2 in this study). The extracted n_{2D} before doping is 1.17×10^{12} cm^{-2}, which is consistent with previous reports. [42,53,68,69] While the extracted n_{2D} after the doping is 1.95×10^{12} cm^{-2}. This doping level (0.78×10^{12} cm^{-2}) is comparable with other doping methods (for example, 2×10^{11} cm^{-2} for OTS doped WSe_2, [44] 4.6×10^{11} cm^{-2} for MEA doped MoS_2, [70] -2×10^{11} cm^{-2} for FDT doped MoS_2, [42] 1×10^{13} cm^{-2} for TiO_x doped graphene). [70] It is noteworthy that due to the ignorance of the coupling between the top oxide layer and bottom gate oxide layer, the C_{ox} after doping is underestimated in our calculations. Thus, the n-doping effect is underestimated as well. The μ_{FE} and n_{2D} of the deivce are extracted at V_{bg} = 30 V. Although the doping effect is independent of the gate voltage, sufficient gate voltage is required to turn

on the channel of the device for accurate measurement. It is noteworthy that the carriers in these transistors are free electrons without the formation of excitons or trions. Because there is no external input to excite electrons to the conduction band and the lifetimes of excitons and trions are too short for transportation, in the order of picoseconds. [11,71]

$$\mu_{FE} = \frac{d}{dV_g} I_{ds} * \frac{L}{W * C_{ox} * V_{ds}}$$ **Equation 3.1**

$$n_{2D} = \frac{I_{ds} * L}{W * \mu_{FE} * V_{ds}}$$

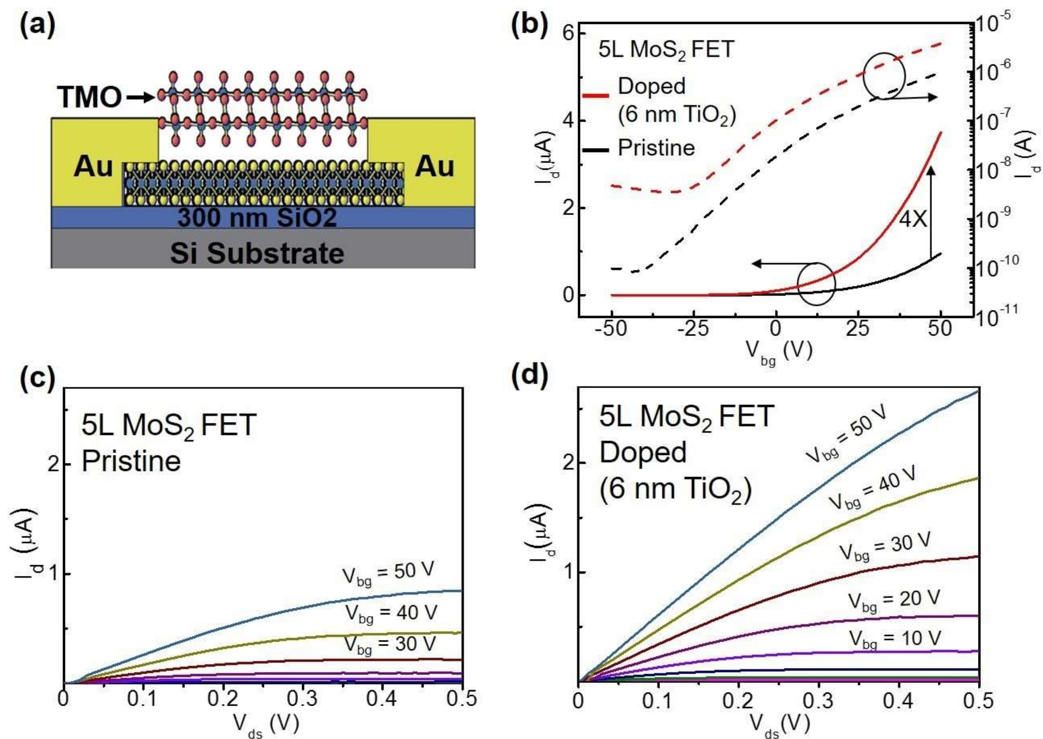

Figure 3.5 Electrical characterizations of MoS_2 FET for n-doping by TiO_2. (a) Cross-sectional schematic of TMO doping MoS_2 FET. (b) Transfer curve of a 5L

MoS_2 FET before (black line) and after (red line) being doped by 6-nm-thick TiO_2. (c) Output curves of the FET before doping; (d) Output curves of the FET after doping.

To further deepen our understanding of the doping effect, DFT calculations were utilized to simulate the doping effect. Anatase phase TiO_2 structure was used in this simulation since it is the stable phase at room temperature. [72] **Figure 3.6**(a) and Figure 3.6(b) show the Atomic and Orbital Projected Density of States of pristine 1H-MoS_2, 1H-MoS_2 in the TiO_2-doped MoS_2 system, anatase TiO_2, and anatase TiO_2 in the TiO_2-doped MoS_2 system, respectively. The bandgap of pristine 1H-MoS_2 is calculated to be ~1.86 eV. Both conduction band minimum (CBM) and valence band maximum (VBM) of MoS_2 are populated by the 4d orbital of Mo atom, which are highly hybridized with the 3p orbital of S atom. These calculation results are highly consistent with acknowledged results of MoS_2. [72] After doping by TiO_2, the Fermi level of 1L MoS_2 is up-shifted by approximately 0.76 eV towards the CBM. This result indicates there is n-doping effect. Also, the bandgap of MoS_2 is obviously shrunken, which is due to the enhanced dielectric screening introduced by TiO_2 deposition. From Figure 3.6(b), we observe a significant change of TiO_2 DOS after doping. Compared with the pristine state, the presence of Ti-5d level in the conduction band is dramatically decreased. This change suggests that electrons are mainly transferred from Ti-5d level of TiO_2 into MoS_2, leaving the Ti-5d level at anti-bonding state.

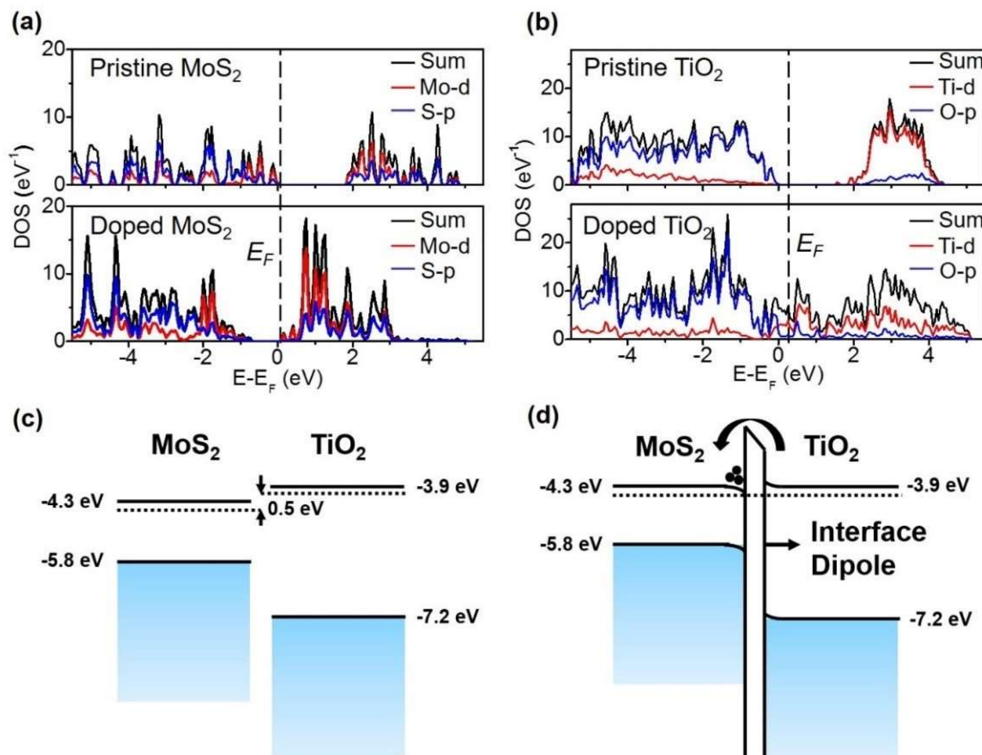

Figure 3.6 DFT simulation results of the n-doping process and band structures of MoS_2 and TiO_2. (a) DOS of 1L 1H-MoS_2 before (upper panel) and after doping (lower panel). (b) DOS of anatase TiO_2 before (upper panel) and after doping MoS_2 (lower panel). (c) Band-alignment of 1L MoS_2 and TiO_2 before doping. (d) Band-alignment of 1L MoS_2 and TiO_2 after doping. The dashed lines denote the CNL.

3.2.3 Layer-dependent p-doping of MoS_2 by MoO_3

MoO_3 is one type of TMO with relatively low CNL. We choose it as the dopant for p-doping MoS_2. **Figure 3.7** shows PL spectra of 1L and 3L MoS_2 before and after 6-nm-thick MoO_3 doping. In both cases, significant decrease of X^- peak spectral weight is observed. The corresponding Raman spectra of these samples are also shown in Figure 3.7. No obvious shift of the Raman frequency is observed,

suggesting that the interlayer coupling between MoO_3 layer and MoS_2 surface is also weak van der Waals interactions. Also, it is noteworthy that the dielectric constant of MoO_3 is small (~5.5). Thus, it only has negligible screening effect on MoS_2 and small influence over the PL spectra of MoS_2.

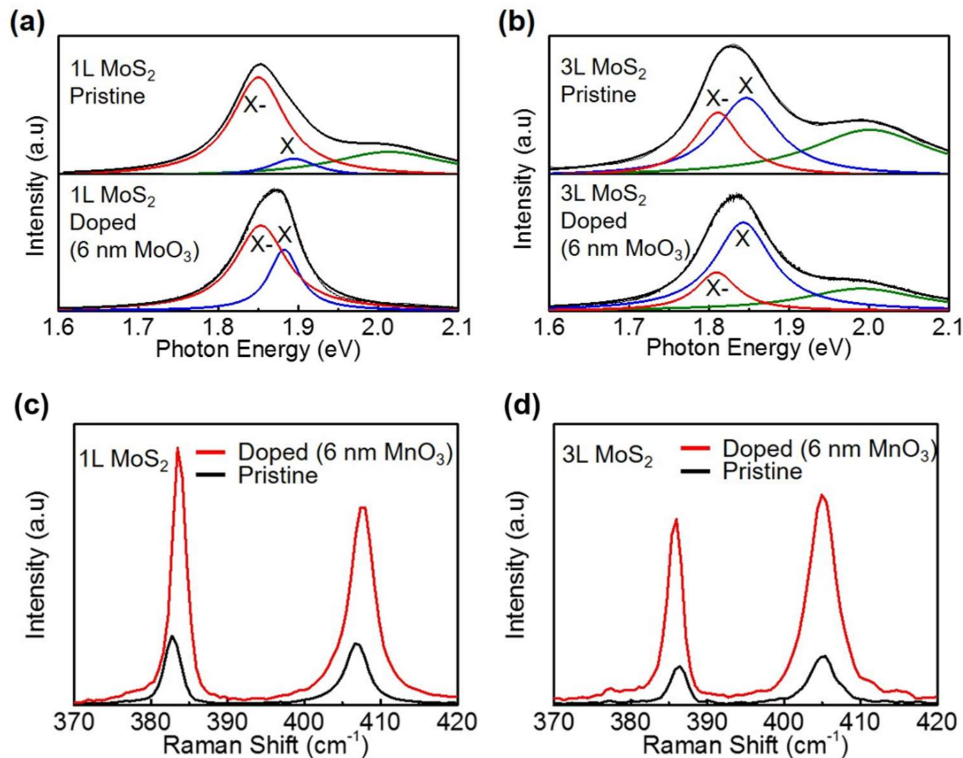

Figure 3.7 PL spectra of ultrathin MoS_2 flakes before and after being doped by 6-nm-thick MoO_3. The thickness of MoS_2 samples are (a) 1L, (b) 3L. Raman spectra of 1L (c) and 3L (d) MoS_2 before (black line) and after (red line) 6-nm-thick MoO_3 doping.

Electrical characterizations of MoS_2 FETs are used to further quantify the p-doping effect. **Figure 3.8**(a) shows the transfer curve of a 5L MoS_2 FET before and after p-doping. After the p-doping, the I_{ON} at V_{bg} = 50 V is decreased by 5

times and the threshold voltage (V_{th}) is increased by ~24 V. The extracted n_{2D} are 2.3 × 101^2 cm^{-2} before the doping and 1.7×10^{12} cm^{-2} after the p-doping. The electron density in MoS_2 is depleted by about 0.6×10^{12} cm^{-2}, which is comparable to the doping level of 6-nm-thick TiO_2 (0.78×10^{12} cm^{-2}). Corresponding output curves of the device are illustrated in Figure 3.8(b) (before doping) and Figure 3.8(c) (after doping). As expected, we observe a decrease of I_{ON} in the positive gate range (0 – 50 V). The gate voltage required to turn on the channel (V_{ON}) is clearly increased from 20 V to 30 V. The n_{2D} and μ_{FE} of MoS_2 devices before and after the p-doping are summarized in Figure 3.8(d). We can see that for thicker MoS_2 samples, the depleted electron density is smaller. This layer-dependence can also be ascribed to the lowering of MoS_2 CNL with the increasing of MoS_2 body thickness. Also, due to the reduced carrier density, electrons undergo stronger scattering effect from the interface defects, which will significantly reduce carrier mobility.

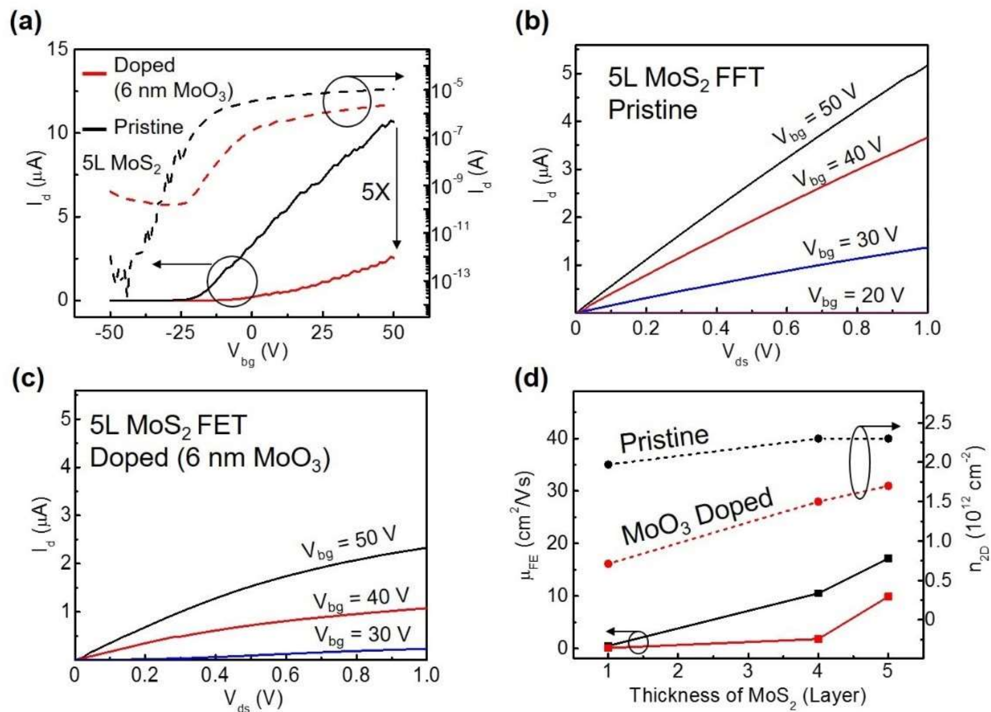

Figure 3.8 Electrical characterizations of MoS_2 FET for p-doping by MoO_3. (a) Transfer curve of a 5L MoS_2 FET before (black line) and after (red line) 6-nm-thick MoO_3 doping. (b) Output curves of the device before doping. (c) Output curves of the device after 6-nm-thick MoO_3 doping. (d) Extracted μ_{FE} (left axis) and n_{2D} (right axis) of three MoS_2 devices before (black line) and after (red line) 6-nm-thick MoO_3 doping.

DFT calculation results of this p-doping process are shown **Figure 3.9**. In Figure 3.9(a), the Fermi level of 1L MoS_2 is moved down towards the VB, demonstrating the p-doping effect. DOS of MoO_3 in Figure 3.9(b) shows that the population of Mo-4d orbital is increased after the doping, indicating that electrons are transferred from the Mo-4d orbital in MoS_2 to the Mo-4d orbital in MoO_3. Figure 3.9(c) illustrates the schematic band-structure of 1L MoS_2 versus MoO_3. The CNL of MoS_2 is 2.2 eV higher than that of MoO_3. Due to this energy difference,

electrons in the CB of MoS_2 are extracted to the CB of MoO_3 until interface dipole is built up (Figure 3.9(d)). When the CNL of MoS_2 is lowered down by increased body thickness, the energy difference between it and the CNL of MoO_3 is decreased. So, for thicker MoS_2, the p-doping effect is decreased.

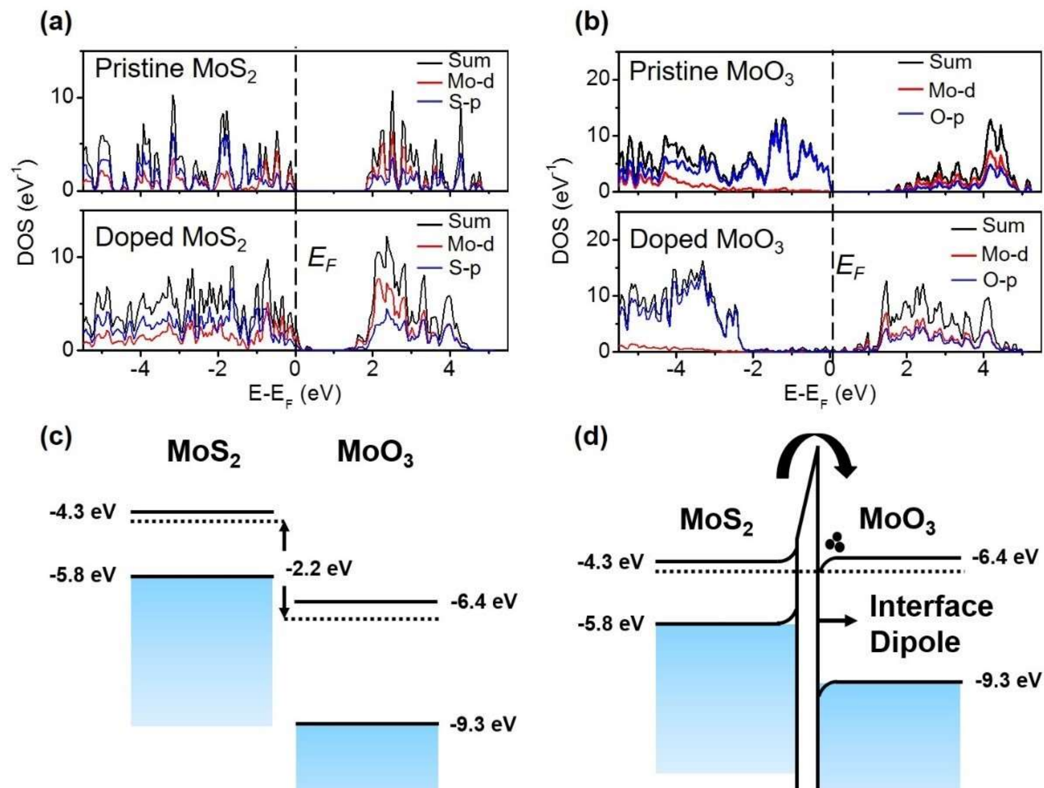

Figure 3.9 DFT simulation results of the p-doping process and band-structures of MoS_2 and MoO_3. (a) DOS of 1L 1H-MoS_2 before (upper panel) and after doping (lower panel). (b) DOS of pristine MoO_3 before (upper panel) and after doping MoS_2 (lower panel). (c) Band-alignment of 1L MoS_2 and MoO_3 before doping. (d) Band-alignment of 1L MoS_2 and MoO_3 after doping. The dashed lines denote the CNL.

3.4 Summary

In summary, we investigate the layer-dependence of n- and p-doping MoS_2

by TMO. TiO_2 and MoO_3 are used for the n- and p-doping of MoS_2, respectively. PL and electrical characterizations show that thicker MoS_2 samples are more easily to be n-doped by TiO_2; while thinner MoS2 samples are more easily to be p-doped by MoO_3. Further, the doping levels of 6-nm-thick TiO_2 and MoO_3 are extracted to be 0.78×10^{12} cm^{-2} and 0.6×10^{12} cm^{-2}, respectively. Our experiments characterized the doping effects and doping levels of the two mostly used oxide dopants (TiO_2 and MoO_3), and shed light on optimizing the doping strategy of 2D materials by oxides layers.

Chapter 4. Optical and Electrical Characterizations of 2D AuSe

4.1 Introduction

Most of the 2D materials like graphene and MoS_2 possess high in-plane symmetry. While some 2D materials like black phosphorus and $ReSe_2$ possess high in-plane asymmetry.[9,73-75] Black phosphorus possesses puckered honeycomb lattice structure with zigzag atomic arrangement along the y-direction. $ReSe_2$ has a low symmetry triclinic crystal structure with Re_4 diamond-shaped chains in plane. The asymmetric atomic arrangements in these materials lead to anisotropic electrical mobility, phonon vibrational modes and photoemission etc. The asymmetric characteristics of 2D materials can have applications in light polarizers, polarization detectors, new types of plasmonic devices etc. The research interest on 2D anisotropic materials has been kindled since the demonstrations of these materials applying in polarized photodetector and digital inverter.[8,76]

Nevertheless, for the most studied 2D anisotropic materials, the in-plane atoms are connected by strong chemical bonding. While for a new emerging type of material which are stacked by atomic ribbons with interchain chemical bonding and intrachain van der Waals interaction. The difference between chemical bonding and van der Waals interaction lead to strong anisotropy in this kind of material. For example, for Sb_2Se_3, the measured hole mobility along the different

direction of it varies for about 3 times.[77] Similar results have also been reported on 2D Tellurium crystals.[78] These studies revealed the potential applications of 2D nanosheets in future electronic and optoelectronic devices.

In this work, we mechanically exfoliate bulk AuSe crystals onto silicon substrates and then perform optical and electrical characterizations for the first time. The vibration modes of α-AuSe are studied both theoretically and experimentally. High anisotropic Raman characteristics have been demonstrated. AuSe FETs have been fabricated and characterized. By electrical characterizations, bulk AuSe is found to have metallic transport characteristics, which is in accordance with our calculation results. Four-point resistivity measurement has shown that AuSe possess high conductivity (σ_{2D} = 0.01 S).

4.2 Experimental Preparations

AuSe single crystals were purchased from commercial producer (HQ graphene). Crystals were cleaved into small pieces and transferred onto Scotch tape. Then samples were transferred onto silicon substrates by attaching the tapes against silicon substrates. Organic residuals from the tape were removed by Acetone/IPA bath. AuSe flakes were identified under optical microscope.

AuSe micro-devices were patterned by photo-lithography and EBL. 5 nm/50 nm Ti/Au electrodes were deposited by electron-beam evaporation at the rate of 0.5 Å /s and 0.7 Å /s, respectively. Electrical characterizations of the AuSe devices were performed by a set of Lakeshore low-temperature I-V probe station and Keithley 4200-SCS semiconductor parameter analyzer.

The Raman and PL spectra of AuSe were collected by a LabRAM HR 800

Raman spectrometer at the excitation length of 488 nm. AuSe flakes were transferred onto copper grids by KOH etching method. TEM characterizations were performed by a Jeol JEM-2011.

4.3 Experiment Results and Discussions

4.3.1 Geometrical and Electronical Structures of α-AuSe

The calculated crystal structure of α-AuSe is shown in **Figure 4.1** (a)-(b). α-AuSe crystallizes in the space group C_{2m} with a = 12.03 Å, b = 3.78 Å and c = 8.45 Å. It is array of parallel atomic chains arranged on a 2D quadrilateral lattice. Bulk AuSe is composed of atomic chains along the b-axis which are bound together by van der Waals interactions along the a-axis and c-axis. These results are in good accordance with previous reports.[19] It is reasonable to interpret that b-axis possesses much higher electrical mobility than the other two directions. Figure 4.1 (c)-(d) show the calculated binding energies along the two Van der Waals directions. The binding energies are calculated to be -0.39 eV and -0.68 eV, respectively. This result indicates that AuSe is more easily to be exfoliated along the c-direction rather than the a-direction.

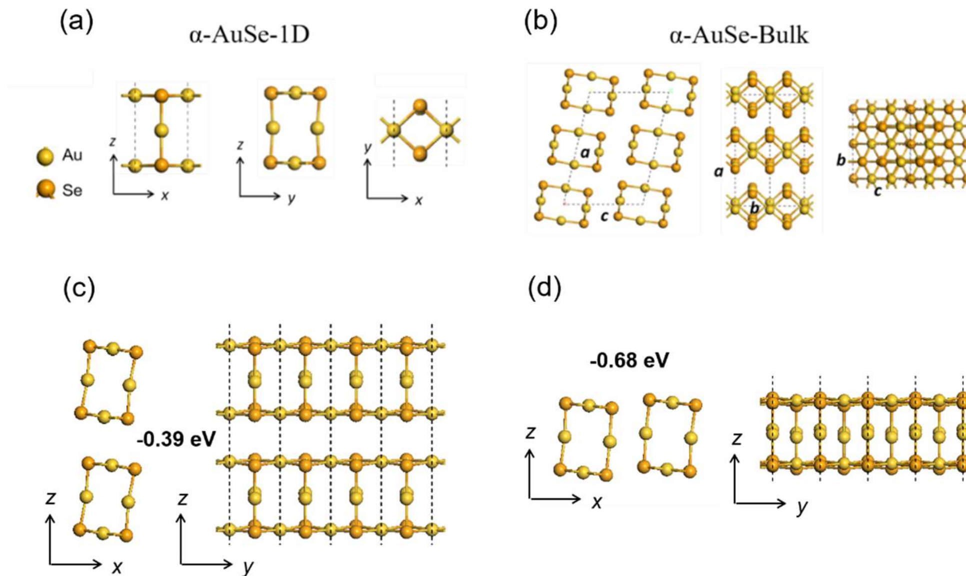

Figure 4.1 Theoretical calculation results of geometrical and electrical structures of α-AuSe. (a)-(b) Geometrical structures of 1D and bulk AuSe, respectively; (c)-(d) Calculated binding energies of Van der Waals interaction along the a-direction and c-direction, respectively.

TEM characterizations have been performed to study the crystal orientation of exfoliated AuSe crystals (**Figure 4.2**). Diffraction pattern in Figure 4.2(a) shows that the AuSe sample is well-crystallized. The spacing between the (400) crystal plane is measured to be 0.29 nm, thus the plane spacing between (100) plane is calculated to be 1.16 nm, which approximates the lattice parameter a (1.22 nm) calculated by our simulations. The crystal orientation of AuSe is illustrated in the insert of Figure 4.2(b). The AuSe crystal is exfoliated along the c-axis. This observation is in good accordance with our simulation results, by which the binding energy along c-direction and a-direction is 0.39 eV and 0.68 eV, respectively. Since the binding energy along the c-direction is much smaller than

that of the a-direction, the AuSe crystal is more easily to be cleaved along the c-direction. The energy-dispersive X-ray (EDX) spectra of AuSe is shown in Figure 4.2(c). The atomic ratio of Au and Se is measured to be around 1:1. It is noteworthy that the Cu element is originated from the Cu grid used for TEM characterizations.

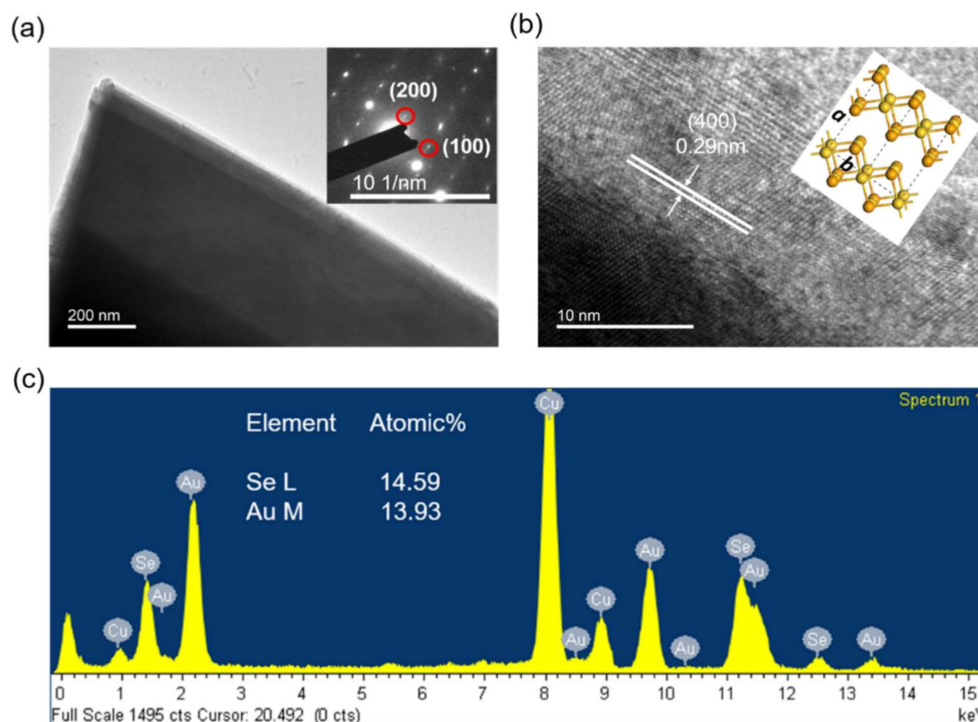

Figure 4.2 TEM characterizations of AuSe. (a) Low-magnification TEM picture of AuSe; the insert shows the selected area diffraction pattern; (b) High magnification TEM picture of AuSe, the insert shows the illustrated atomic alignment; (c) EDX spectroscopy of AuSe.

4.3.3 Raman Spectra of α-AuSe

Raman is a statistical and non-destructive characterization method of crystal lattice structure and lattice vibration modes. In addition to the TEM

characterizations of AuSe, both of calculation and experiments have been performed to study the Raman spectra of AuSe. Table 4.1 summarizes the calculated results of AuSe vibration modes. A total number of 21 modes are discovered, among which 12 modes are found to be Raman active.

Table 4.1. Calculated vibration modes of α-AuSe. The modes are classified into Infrared active (I) vibration mode and Raman active (R) vibration mode.

Mode	Frequency (cm^{-1})	Infrared (I) or Raman (R) Active
1	217.98	I
2	211.30	I
3	210.14	R
4	209.80	I
5	208.37	R
6	208.22	R
7	198.45	R
8	190.05	R
9	181.12	I
10	176.77	I
11	160.86	R
12	146.75	I
13	82.50	I
14	67.31	R
15	60.48	I
16	58.90	I
17	53.69	R
18	48.29	R
19	35.11	R
20	20.39	R
21	18.17	R

Collected Raman spectra (both low-frequency and high frequency) of bulk AuSe are shown in Figure 4.3. In the low-frequency region, 3 peaks are identified (16.65 cm^{-1}, 34.5 cm^{-1}, 77.29 cm^{-1}). Four peaks in the high-frequency region are identified (177.81 cm^{-1}, 199.68cm^{-1}, 208.14 cm^{-1}, 216.42cm^{-1}), which are referenced as peak A, B, C, D in this thesis, respectively. The experimental results match well with the calculation results. Except for the peak A and peak D, which are calculated to be only infrared-active. Due to the prominent intensity of peak A, it cannot be asserted to be originated from experimental errors. This discrepancy between theoretical and experimental results need to be addressed. It is noteworthy that no layer-dependence of Raman peaks is observed in our experiments.

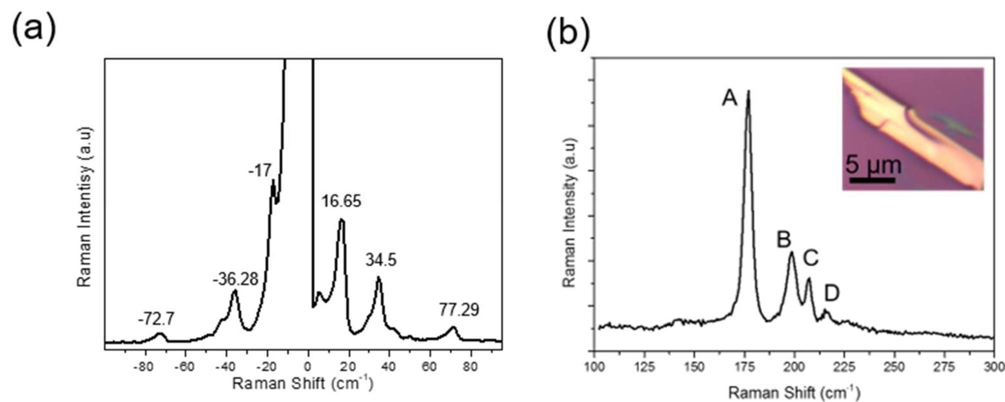

Figure 4.3. Collected Raman spectra of bulk AuSe, including the low-frequency part (a) and high-frequency part.

Due to the highly anisotropic atomic structure of AuSe, the lattice vibrations of AuSe are predicted to be polarized. Thus, polarized Raman spectra have been conducted to demonstrate the polarization of Raman peaks. Among high-

frequency Raman peaks, peak B and peak C are found to be highly polarized. The intensity of peak B and peak C versus the polarization angles of incident laser are presented in **Figure 4.4**. For polarized Raman spectra, the polarization angle of incident laser is referenced so that the b-axis (along the atomic chain direction) corresponds with the angle of 90˚. The vibration modes of peak B and peak C are also calculated and illustrated. Figure 4.4(a) shows that the peak B originates from the lattice vibrations in the XZ plane and it exhibits a minimum intensity at the polarization angle of 35˚ and a maximum intensity at the polarization angle of 125˚ (Figure 4.4(b)); while peak C is originated from the lattice vibration perpendicular to the XZ plane and it exhibits a maximum intensity at 45˚ and a minimum intensity at 120˚. The intensity ratio of peak B varied by about 3 times and the intensity ratio of peak C varied by about 6 times. Thus, this demonstrates the strong anisotropy of the lattice vibrations in AuSe crystal, which is originated from the difference between chemical bonding along the b-axis and van der Waals interactions along the a-axis. It is noteworthy that the Raman intensity of peak D is not collected nor analyzed in the polarized Raman spectra because of its extremely low intensity.

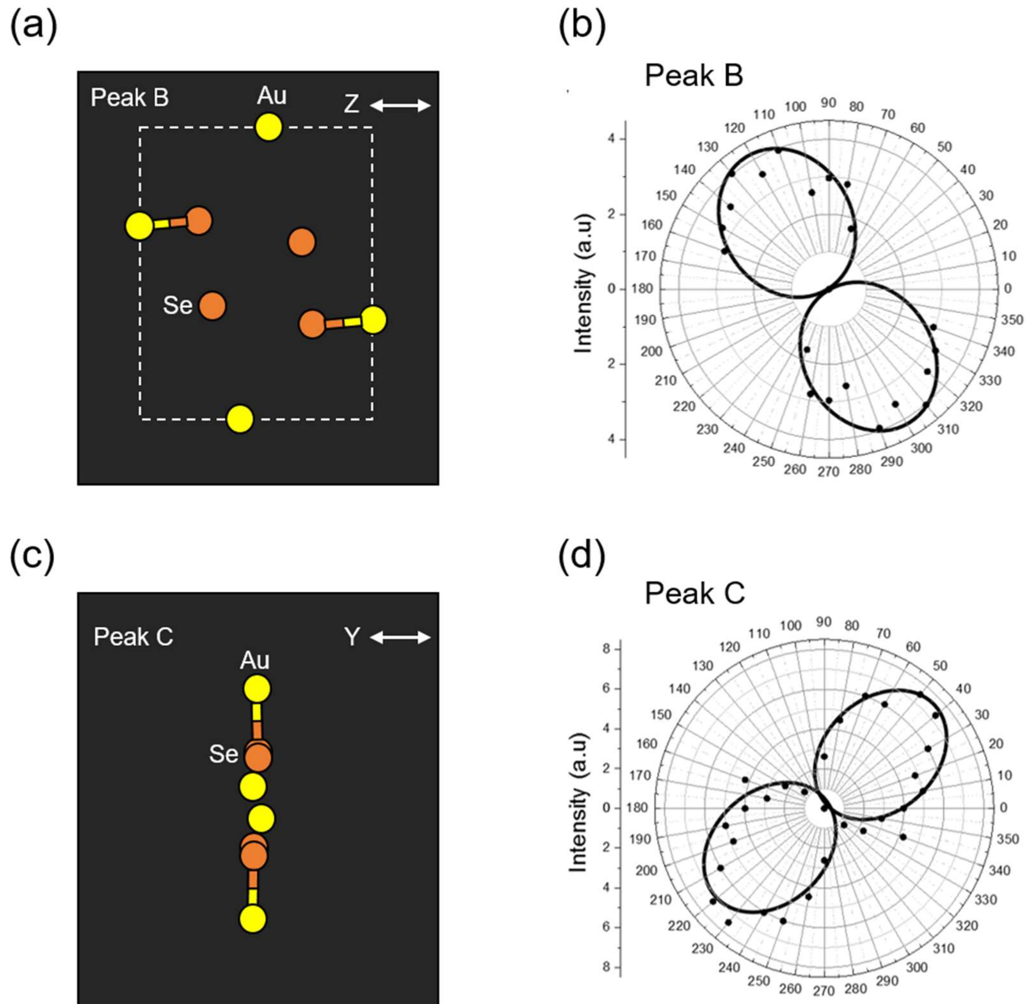

Figure 4.4. Polarization of peak B and peak C. The schematic of vibration mode of peak B (a) and the intensity of peak B versus polarization angle (b); The schematic of vibration mode of peak C (c) and the intensity of peak C versus polarization angle.

To explore the structural change of AuSe under low-temperature, we performed temperature-dependent Raman of bulk AuSe, as shown in **Figure 4.5**. The frequency of all Raman active peaks blue-shift for about 5 cm^{-1} when temperature decreases from 20 °C to -180 °C. This is due to the an-harmonic contributions from inter-atomic interactions. More intuitively, this is due to the

coupling effect of the change of in-cell pressure and cell parameters originated from the thermal expansion effect. Similar results and detailed analysis of MoS_2 has been report.[79] Beside this, there is no significant change of Raman spectra, which demonstrates that there is no obvious structural change in this temperature range.

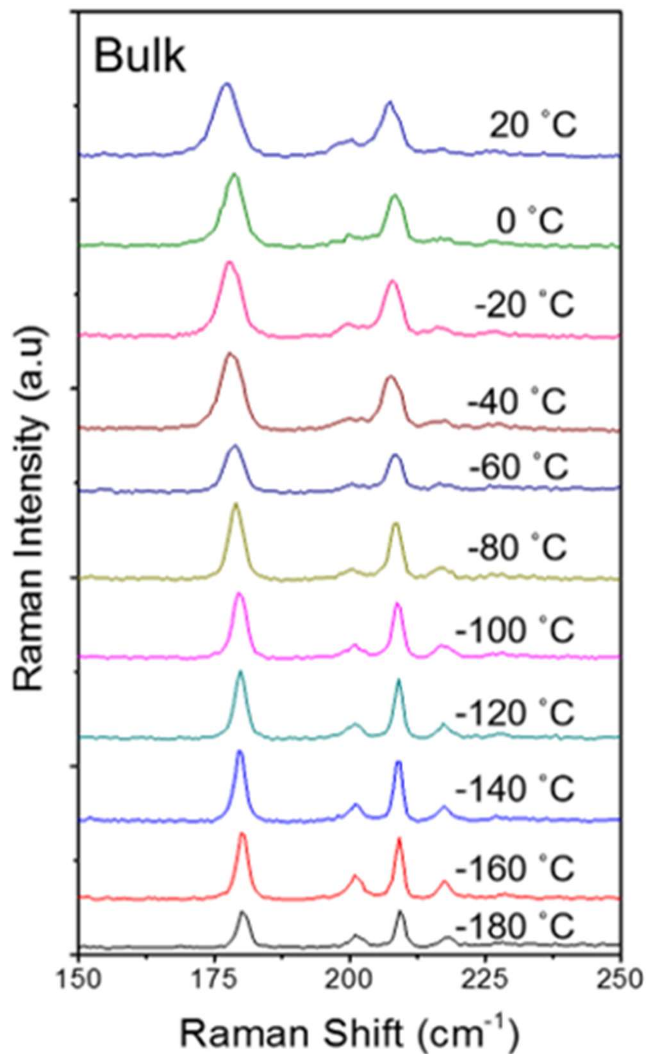

Figure 4.5 Low-temperature Raman of bulk AuSe from 20 °C to -180 °C.

4.3.4 Electrical Transport Properties of α-AuSe

Figure 4.6 (a)-(b) show the calculated electronic structures of one-dimensional (1D) α-AuSe and bulk α-AuSe. 1D AuSe is calculated to be semiconductor with an indirect bandgap of 1.26 eV, which is comparable with other most studied 2D materials. The bandgap corresponds to a wavelength of 984 nm, which lies in the near-infrared region. The appropriate bandgap enables AuSe to be applied as channel material in a FET, infrared photodetectors, etc. On the other hand, bulk AuSe is calculated to be metallic with no bandgap. The conduction band and valence band overlap in the directions of G-Y and Q-Z. The metal-insulator transition (MIT) from bulk α-AuSe to 1D-AuSe indicates there is strong inter-layer interactions.

Bulk AuSe FETs are fabricated and characterized at room temperature. Figure 4.6 (c) shows the transfer curve of the bulk AuSe FET. We can see that this device shows metallic behavior. The channel cannot be turned off and it shows no on/off ratio during the gate voltage from – 50 V to 50 V with a drain to source voltage of 100 mV. The drain to source current is relative large (25 μA) comparing with other low-dimensional materials, *i.e.*, MoS_2 (< 1 μA at the same conditions). Figure 4.6 (d) shows the output curves of the device. The arrow indicates the increase of gate voltage from -50 V to 50 V with a step of 10 V. Also, we observe weak on/off ratio and the device shows large conductivity. The metallic transport behavior of bulk AuSe is consistent with our simulation results. The output curves of bulk AuSe at 300 K, 200 K and 100 K are shown in Figure 4.6 (d)-(f). The current through source and drain decreases with decreasing temperature when the other conditions

remain the same. At the same time, the output curves become more unlinear when temperature decreases. We think this is due to the degradation of the contacts between electrodes and AuSe, which is originated from the change of lattice parameters when temperature decreases.

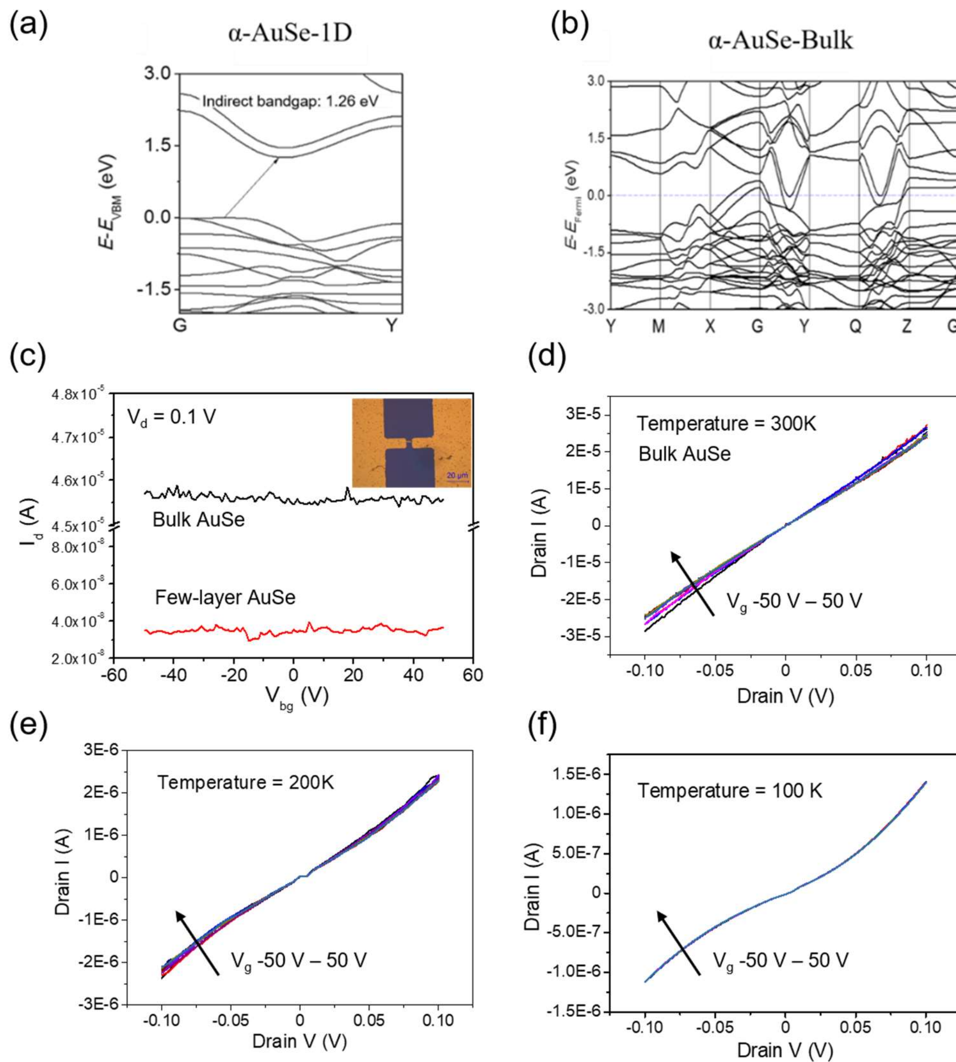

Figure 4.6 Calculations and characterizations of the electronic structure of AuSe. Calculated bandgap of 1D (a) and bulk (b) AuSe. (c) Transfer curve of both bulk and few-layer AuSe FET under room temperature. (d)-(f) Output curves of bulk AuSe FET under 300 K, 200 K and 100 K, respectively.

Four-point resistance measurement has been performed to quantitatively

demonstrate the intrinsic metallic transport behavior of bulk AuSe. A four-point structure of bulk AuSe has been fabricated and tested under the temperature ranging from 193 K to 50 K. **Figure 4.7**(a) shows the cross-sectional schematic of a four-point structure. A constant current flow is introduced by the first and last electrodes through the channel material. The inner two electrodes measure the voltage drop in the channel material with a high impedance. Because the current through the inner electrodes is negligible, the contact barrier between the channel material and electrodes are excluded from the voltage difference between the two inner electrodes. So, the measurement results reveal the intrinsic properties of the channel material, without influences from the electrode contacts. Figure 4.7(b) shows the extracted 2D sheet conductivity (σ_{2D}) of both bulk and thin AuSe versus temperature. For bulk AuSe, the σ_{2D} increases from 2.5×10^{-3} S at 193 K to 1.3×10^{-2} S at 50 K; for few-layer AuSe, the σ_{2D} increases from 2.8×10^{-4} S at 193 K to 3.2×10^{-4} S at 50 K. Conductivity of a material is dependent on both the carrier concentration and carrier mobility. In this case, it is reasonable to interpret AuSe as metal. Because for metals, the carrier concentration has negligible dependence on the temperature; and the carrier mobility increases with decreasing temperature due to reduced thermal phonon scattering. So, the AuSe device behaves like a metal for its conductivity increases with decreasing temperature. On the other hand, if AuSe is semiconductor, it will exhibit decreased conductivity with decreasing temperature. Because for semiconductors, the conductivity is largely dependent on the carrier concentration. When temperature decreases, less number of electrons are excited to the conduction band. At the same time, it is noteworthy that the

conductivity of bulk AuSe (2.5×10^{-3} S) is comparable to that of bulk $PtSe_2$ (~10^{-2} S).[7] This enables the potential applications of bulk AuSe as low-resistance contacts in 2D circuits.

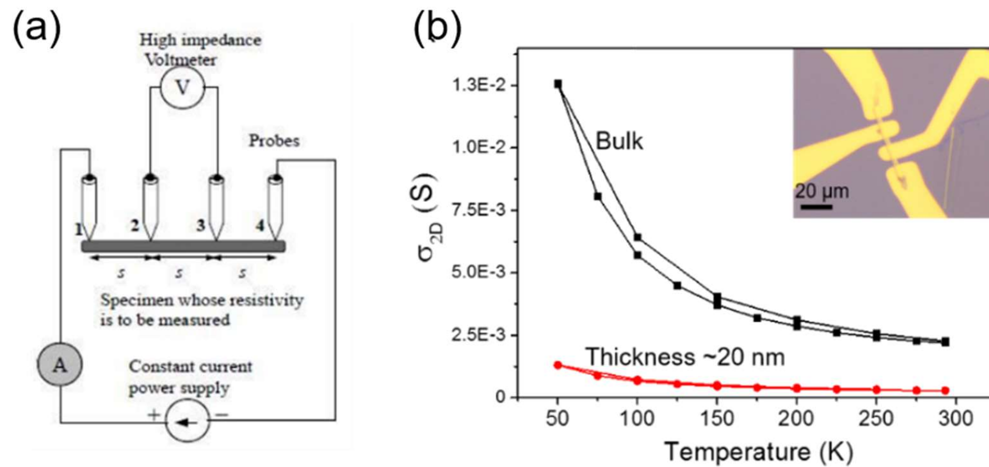

Figure 4.7 Four-point electrical characterization results of α-AuSe. (a) Schematic of four-point resistivity measurement; (b) Extracted 2D sheet conductivity of bulk AuSe (black) and thin AuSe (red) versus temperature. The inset shows the optical microscope image of the bulk AuSe device with four-point configuration.

4.4 Summary

In summary, theoretical calculations, optical and electrical characterizations have been performed for 2D AuSe for the first time. AuSe is composed of parallel atomic chains via weak van der Waals interactions. Raman spectra of AuSe is performed and the results have good accordance with the calculation results. Polarized Raman spectra is conducted for bulk α-AuSe. Strong anisotropy of Raman peaks is found. Low-temperature raman spectra of α-AuSe in the range of 20 °C to -180 °C shows there is no significant change of the crystal structure during

this temperature range.1D α-AuSe is calculated to be semiconductor with an indirect bandgap ~ 1.26 eV; bulk α-AuSe is calculated to be semi-metal with conduction band and valence band overlaps in the directions of G-Y and Q-Z. Bulk α-AuSe FETs show high 2D-sheet carrier conductivity (~10^{-2} S) and weak gate modulation. Four-point resistivity measurement over the temperature from 193 K to 50 K demonstrates that both bulk and few-layer α-AuSe are semi-metals.

Chapter 5. Conclusions and Outlook

5.1 Conclusions

2D materials are layered materials with weak interlayer Van der Waals interactions. Different from traditional bulk materials, 2D materials can be thinned down to the thickness of a single layer without dangling bonds. Because of their unique electronic, optical and optoelectronic properties, 2D materials have been under great research interest since the first demonstration of graphene in 2004.[1-5]

The modulation doping of 2D materials provides a way to change their physical properties in a controllable manner. The interaction between carrier and exciton enables additional path for photoluminescence (PL) modulation of 2D materials. By controlling the carrier type and density through modulation doping, it provides a way to switch between exciton and trion dominant PL and tune the PL intensity of 2D materials. Controllable injection and extraction of electrons/holes are important for effective n- and p-doping of 2D materials, which is crucial for building complementary logic circuits in the future.

Ion-implantation is a well-established and widely-used doping technology in the current semiconductor industry. The dopant profile and dopant depth can be tuned by implantation energy and fluence.[51,52] Extending this matured doping technology from Si semiconductor to 2D materials will minimize the cost for establishing new infrastructures and maximize the effectiveness. However, the implantation energy of conventional implanters is usually high (> 10 keV) for

ultrathin 2D materials. Applying this type of implanter to 2D materials directly causes severe lattice damage and only lead to very low retention. In the first part of this work, we demonstrate a method to directly utilize traditional ion-implanter to dope 2D materials. A thin layer (200 nm or 1000 nm) of PMMA was spin-coated onto ultrathin MoS_2 flakes as a sacrificial layer. The PMMA layer decelerates the dopant ions and successfully retains a portion of dopant ions inside the 2D MoS_2 flakes. Phosphorus was selected as the dopant since it has one electron less than sulfur and has high affinity for molybdenum in sulfur-deficient MoS_2. Phosphorus ions were implanted with an implantation energy of 10 keV and a fluence of $5x10^{13}$ cm^{-2}. The PMMA layer was then washed away by acetone and Isopropyl Alcohol (IPA) after the implantation process. Raman spectra and High Resolution TEM (HRTEM) show that there is no obvious damage to the MoS_2 lattice. Photoluminescence (PL) and electrical characterizations show that few-layer MoS_2 flakes are successfully p-doped by incorporated phosphorus atoms. HRTEM and electron diffraction pattern reveal that the crystal structure of 2D MoS_2 remained well after implantation. By analyzing Raman spectra of MoS_2, it is suggested that the major of implanted ions is deaccelerated by the top few layers of MoS_2 while the underlying layers are less affected. PL spectra of ultrathin MoS_2 show significant p-doping effect in relative thick samples (> 3L). The p-doping effect is also demonstrated by FET characterizations. The ON-current is decreased and threshold voltage is up-shifted in Phosphorus-implanted few-layer MoS_2 FET. The dopant depth can be adjusted by varying the thickness of PMMA. Thinner PMMA leads to larger kinetic damage but also more significant doing effect. Also,

the kinetic damage could be effectively reduced by increasing the thickness of MoS_2. This doping strategy is compatible with state-of-the-art CMOS technologies and can be used for large-scale manufacturing. Also, this method could also be applied to other 2D materials as well.

In the second part of this work, we use transition metal oxide (TMO) to modulation dope 2D MoS_2 by surface charge transfer. We deposit TMO on top of 2D MoS_2 to form a heterojunction device. We choose TiO_2 with high charge neutrality level (CNL) and MoO_3 with low CNL for injecting and extracting electrons, respectively. We observe effective modulation of MoS_2 PL spectra by this doping method. TiO_2 induced n-doping of MoS_2 increases the negative trion ratio; while MoO_3 induced p-doping of MoS_2 decreases the negative trion ratio. Raman spectra show only small broaden or shift after doping, which means negligible damage to MoS_2 lattice is introduced during the doping process. By electrical characterizations of MoS_2 field-effect-transistors (FETs), the doping levels of 6-nm-thick TiO_2 and MoO_3 are extracted to be 0.78×10^{12} cm^{-2} and 0.6×10^{12} cm^{-2}, respectively. This doping level is comparable with other doping methods. In addition, we also reveal layer-dependent PL and doping effects in 2D layered MoS_2. PL and electrical characterizations show that thicker MoS_2 samples are more easily to be n-doped by TiO_2; while thinner MoS_2 samples are more easily to be p-doped by MoO_3. Our experiments characterized the doping effects and doping levels of the two mostly used oxide dopants (TiO_2 and MoO_3), and shed light on optimizing the doping strategy of 2D materials by oxides layers. This approach opens a way to control the characteristics of PL and electrical transport

of 2D layered materials.

Due to strong anisotropic characteristics, materials composed of atomic chains via van der Waals interactions has gained much research interest in recent years.[77] AuSe is one type of this material which has not been studied yet. In the third part of this study, the optical and electrical properties of 2D α-AuSe are studied by both theoretical calculations and experiments. Four high-frequency Raman peaks of α-AuSe are identified and have been demonstrated to have high in-plane anisotropy. Low-temperature raman spectra of α-AuSe in the range of 20 °C to -180 °C shows there is no significant change of the crystal structure during this temperature range. 1D α-AuSe is calculated to be semiconductor with an indirect bandgap ~ 1.26 eV; bulk α-AuSe is calculated to be semi-metal. Bulk α-AuSe FETs show high 2D-sheet carrier conductivity (~10^{-2} S) and weak gate modulation. Four-point resistivity measurement demonstrates that α-AuSe exhibits metallic transport properties.

5.2 Outlook

Although effective p-doping effects have been observed in PMMA-assisted ion-implantation of MoS_2 in this study. Future works are needed to reveal the concentration profile of dopant ions along the cross-section of host material and its dependency on the external implantation parameters, *i.e.*, implantation energy and the thickness of PMMA layer. This will deepen our understanding about the doping process and help optimize the doping parameters.

The oxygen vacancies play an important role in modulating the CNL of TMO, thus changing the doping effect of TMO.[72] Theoretical simulations and

experimental quantifications are required to further understand the effects of oxygen vacancies introduced into various TMOs. Further studies are needed to monitor and modify the CNL of TMO in a controllable manner to adjust the doping effects.

The vibrational modes of α-AuSe have not been fully understood yet. Further calculations and experiments need to be performed to reveal it. The in-plane anisotropy if 2D α-AuSe will be further demonstrated and quantified by polarized electrical measurements. Also, magneto-transport measurements will be carried out to exploit the unique band-structure of bulk AuSe.

References

1 Radisavljevic, B., Radenovic, A., Brivio, J., Giacometti, i. V. & Kis, A. Single-layer MoS_2 transistors. *Nature nanotechnology* **6**, 147-150 (2011).

2 Zhou, C. *et al.* Carrier Type Control of WSe_2 Field-Effect Transistors by Thickness Modulation and MoO_3 Layer Doping. *Advanced Functional Materials* (2016).

3 Zhao, Y. *et al.* Extraordinarily Strong Interlayer Interaction in 2D Layered PtS_2. *Advanced Materials* (2016).

4 Lin, Z. *et al.* Controllable Growth of Large–Size Crystalline MoS_2 and Resist-Free Transfer Assisted with a Cu Thin Film. *Scientific reports* **5** (2015).

5 Zhou, C. *et al.* Low voltage and high ON/OFF ratio field-effect transistors based on CVD MoS_2 and ultra high-k gate dielectric PZT. *Nanoscale* **7**, 8695-8700 (2015).

6 Young, K. K. Short-channel effect in fully depleted SOI MOSFETs. *IEEE Transactions on Electron Devices* **36**, 399-402 (1989).

7 Zhao, Y. *et al.* High-Electron-Mobility and Air-Stable 2D Layered $PtSe_2$ FETs. *Advanced Materials* **29** (2017).

8 Liu, E. *et al.* Integrated digital inverters based on two-dimensional anisotropic ReS_2 field-effect transistors. *Nature communications* **6** (2015).

9 Wang, X. *et al.* Highly anisotropic and robust excitons in monolayer black phosphorus. *Nature nanotechnology* **10**, 517-521 (2015).

10 Lin, Y. *et al.* Dielectric screening of excitons and trions in single-layer MoS_2. *Nano letters* **14**, 5569-5576 (2014).

11 Wang, Q. *et al.* Valley carrier dynamics in monolayer molybdenum disulfide from helicity-resolved ultrafast pump–probe spectroscopy. *ACS nano* **7**, 11087-11093 (2013).

12 Zhang, Y., Tan, Y.-W., Stormer, H. L. & Kim, P. Experimental observation of quantum Hall effect and Berry's phase in graphene. *arXiv preprint cond-mat/0509355* (2005).

13 Bernardi, M., Palummo, M. & Grossman, J. C. Extraordinary sunlight absorption and one nanometer thick photovoltaics using two-dimensional monolayer materials. *Nano letters* **13**, 3664-3670 (2013).

14 Splendiani, A. *et al.* Emerging photoluminescence in monolayer MoS_2. *Nano letters* **10**, 1271-1275 (2010).

15 Mak, K. F., He, K., Shan, J. & Heinz, T. F. Control of valley polarization in monolayer MoS_2 by optical helicity. *Nature nanotechnology* **7**, 494-498 (2012).

16 Mak, K. F. *et al.* Tightly bound trions in monolayer MoS_2. *Nature materials* **12**, 207-211 (2013).

17 Carvalho, A., Ribeiro, R. & Neto, A. C. Band nesting and the optical response of two-dimensional semiconducting transition metal dichalcogenides. *Physical Review B* **88**, 115205 (2013).

18 Kozawa, D. *et al.* Photocarrier relaxation in two-dimensional semiconductors. *arXiv preprint arXiv:1402.0286* (2014).

19 Rabenau, A. & Schulz, H. The crystal structures of α-AuSe and β-AuSe. *Journal of the Less Common Metals* **48**, 89-101 (1976).

20 Suh, J. *et al.* Doping against the native propensity of MoS_2: degenerate hole doping by cation substitution. *Nano letters* **14**, 6976-6982 (2014).

21 Wei, D. *et al.* Synthesis of N-doped graphene by chemical vapor deposition and its electrical properties. *Nano letters* **9**, 1752-1758 (2009).

22 Zhao, Y. *et al.* Doping, Contact and Interface Engineering of Two-Dimensional Layered Transition Metal Dichalcogenides Transistors. *Advanced Functional Materials*, doi:10.1002/adfm.201603484 (2016).

23 Åhlgren, E., Kotakoski, J. & Krasheninnikov, A. Atomistic simulations of the implantation of low-energy boron and nitrogen ions into graphene. *Physical Review B* **83**, 115424 (2011).

24 Bangert, U. *et al.* Ion Implantation of Graphene Toward IC Compatible Technologies. *Nano letters* **13**, 4902-4907 (2013).

25 Willke, P. *et al.* Doping of graphene by low-energy ion beam implantation: structural, electronic, and transport properties. *Nano letters* **15**, 5110-5115 (2015).

26 Xu, Y., Zhang, K., Brüsewitz, C., Wu, X. & Hofsäss, H. C. Investigation of the effect of low energy ion beam irradiation on mono-layer graphene. *AIP Advances* **3**, 072120 (2013).

27 Willke, P. *et al.* Short-range ordering of ion-implanted nitrogen atoms in SiC-graphene. *Applied Physics Letters* **105**, 111605 (2014).

28 Murray, R. *et al.* The Effect of Low Energy Ion Implantation on MoS_2. *ECS Journal of Solid State Science and Technology* **5**, Q3050-Q3053 (2016).

29 Chen, M. *et al.* Stable few-layer MoS_2 rectifying diodes formed by plasma-assisted doping. *Applied Physics Letters* **103**, 142110 (2013).

30 Wi, S. *et al.* Enhancement of photovoltaic response in multilayer MoS_2 induced by plasma doping. *ACS nano* **8**, 5270-5281 (2014).

31 Lin, Y.-C., Lin, C.-Y. & Chiu, P.-W. Controllable graphene N-doping with ammonia plasma. *Applied Physics Letters* **96**, 133110 (2010).

32 Nipane, A., Karmakar, D., Kaushik, N., Karande, S. & Lodha, S. Few Layer MoS_2 p-Type Devices Enabled by Selective Doping Using Low Energy Phosphorus Implantation. *ACS nano* (2016).

33 Ou, J. Z. *et al.* Physisorption-based charge transfer in two-dimensional SnS_2 for selective and reversible NO_2 gas sensing. *ACS nano* **9**, 10313-10323 (2015).

34 Tongay, S. *et al.* Broad-range modulation of light emission in two-dimensional semiconductors by molecular physisorption gating. *Nano letters* **13**, 2831-2836 (2013).

35 Ovcharenko, R., Dedkov, Y. & Voloshina, E. Adsorption of NO_2 on WSe_2: DFT and photoelectron spectroscopy studies. *Journal of Physics:*

Condensed Matter **28**, 364003 (2016).
36 Fang, H. *et al.* High-performance single layered WSe_2 p-FETs with chemically doped contacts. *Nano letters* **12**, 3788-3792 (2012).
37 Zhao, P. *et al.* Air stable p-doping of WSe_2 by covalent functionalization. *ACS nano* **8**, 10808-10814 (2014).
38 Huo, N. *et al.* Photoresponsive and gas sensing field-effect transistors based on multilayer WS_2 nanoflakes. *Scientific reports* **4**, 5209 (2014).
39 Cho, B. *et al.* Charge-transfer-based gas sensing using atomic-layer MoS_2. *Scientific reports* **5** (2015).
40 Kang, D. H. *et al.* High-Performance Transition Metal Dichalcogenide Photodetectors Enhanced by Self-Assembled Monolayer Doping. *Advanced Functional Materials* **25**, 4219-4227 (2015).
41 Son, Y. *et al.* Observation of switchable photoresponse of a monolayer WSe_2–MoS_2 lateral heterostructure via photocurrent spectral atomic force microscopic imaging. *Nano letters* **16**, 3571-3577 (2016).
42 Sim, D. M. *et al.* Controlled Doping of Vacancy-Containing Few-Layer MoS_2 via Highly Stable Thiol-Based Molecular Chemisorption. *ACS nano* **9**, 12115-12123 (2015).
43 Du, Y., Liu, H., Neal, A. T., Si, M. & Peide, D. Y. Molecular Doping of Multilayer MoS_2 Field-Effect Transistors: Reduction in Sheet and Contact Resistances. *IEEE Electron Device Letters* **34**, 1328-1330 (2013).
44 Kang, D.-H. *et al.* Controllable nondegenerate p-type doping of tungsten diselenide by octadecyltrichlorosilane. *ACS nano* **9**, 1099-1107 (2015).
45 Kiriya, D., Tosun, M., Zhao, P., Kang, J. S. & Javey, A. Air-stable surface charge transfer doping of MoS_2 by benzyl viologen. *Journal of the American Chemical Society* **136**, 7853-7856 (2014).
46 Lee, I. *et al.* Non-degenerate n-type doping by hydrazine treatment in metal work function engineered WSe_2 field-effect transistor. *Nanotechnology* **26**, 455203 (2015).
47 Yamamoto, M., Nakaharai, S., Ueno, K. & Tsukagoshi, K. Self-Limiting Oxides on WSe2 as Controlled Surface Acceptors and Low-Resistance Hole Contacts *Nano letters* **16**, 2720-2727, doi: 10.1021/acs.nanolett.6b00390 (2016).
48 Kaushik, N., Karmakar, D., Nipane, A., Karande, S. & Lodha, S. Interfacial n-Doping Using an Ultrathin TiO_2 Layer for Contact Resistance Reduction in MoS2. *Acs Applied Materials & Interfaces* **8**, 256-263, doi:10.1021/acsami.5b08559 (2016).
49 McDonnell, S. *et al.* Hole Contacts on Transition Metal Dichalcogenides: Interface Chemistry and Band Alignments. *ACS Nano* **8**, 6265-6272, doi:10.1021/nn501728w (2014).
50 Rai, A. *et al.* Air Stable Doping and Intrinsic Mobility Enhancement in Monolayer Molybdenum Disulfide by Amorphous Titanium Suboxide Encapsulation. *Nano letters* **15**, 4329-4336, doi:10.1021/acs.nanolett.5b00314 (2015).
51 Williams, J. Ion implantation of semiconductors. *Materials Science and Engineering: A* **253**, 8-15 (1998).

52 Park, H.-Y. *et al.* Wide-range controllable n-Doping of molybdenum disulfide (MoS_2) through thermal and optical activation. *ACS nano* **9**, 2368-2376 (2015).

53 Ion implantation // Physical encyclopedia (in Russian). V. 2 / Ed. by A.M. Prokhorov. — Moscow: Sovetskaja ehnciklopedija, 1990. 197–199 pp.

54 Rubin L, Poate J. Ion implantation in silicon technology [J]. Industrial Physicists, 2003, 9(3): 12-15

55 Porte, L., De Villeneuve, C. & Phaner, M. Scanning tunneling microscopy observation of local damages induced on graphite surface by ion implantation. *Journal of Vacuum Science & Technology B: Microelectronics and Nanometer Structures Processing, Measurement, and Phenomena* **9**, 1064-1067 (1991).

56 Nipane, A., Karmakar, D., Kaushik, N., Karande, S. & Lodha, S. Few-layer MoS_2 p-type devices enabled by selective doping using low energy phosphorus implantation. *ACS nano* **10**, 2128-2137 (2016).

57 Li, H. *et al.* From bulk to monolayer MoS_2: evolution of Raman scattering. *Advanced Functional Materials* **22**, 1385-1390 (2012).

58 Chakraborty, B., Matte, H., Sood, A. & Rao, C. Layer-dependent resonant Raman scattering of a few layer MoS_2. *Journal of Raman Spectroscopy* **44**, 92-96 (2013).

59 Kaushik, N., Karmakar, D., Nipane, A., Karande, S. & Lodha, S. Interfacial n-Doping using an Ultra-Thin TiO_2 Layer for Contact Resistance Reduction in MoS_2. *ACS applied materials & interfaces* (2015).

60 Berghäuser, G. & Malic, E. Analytical approach to excitonic properties of MoS_2. *Physical Review B* **89**, 125309 (2014).

61 Mouri, S., Miyauchi, Y. & Matsuda, K. Tunable photoluminescence of monolayer MoS_2 via chemical doping. *Nano letters* **13**, 5944-5948 (2013).

62 Singh, A. *et al.* Trion formation dynamics in monolayer transition metal dichalcogenides. *Physical Review B* **93**, 041401 (2016).

63 Liu, D., Guo, Y., Fang, L. & Robertson, J. Sulfur vacancies in monolayer MoS_2 and its electrical contacts. *Applied Physics Letters* **103**, 183113 (2013).

64 Rotunno, E. *et al.* Structural, optical and compositional stability of MoS_2 multi-layer flakes under high dose electron beam irradiation. *2D Materials* **3**, 025024 (2016).

65 Chen, X. *et al.* Probing the Electron States and Metal-Insulator Transition Mechanisms in Atomically Thin MoS_2 Based on Vertical Heterostructures. *arXiv preprint arXiv:1407.5365* (2014).

66 Cheiwchanchamnangij, T. & Lambrecht, W. R. Quasiparticle band structure calculation of monolayer, bilayer, and bulk MoS_2. *Physical Review B* **85**, 205302 (2012).

67 Yang, L. *et al.* Lattice strain effects on the optical properties of MoS_2 nanosheets. *Scientific reports* **4**, 5649 (2014).

68 Das, S., Chen, H.-Y., Penumatcha, A. V. & Appenzeller, J. High performance multilayer MoS_2 transistors with scandium contacts. *Nano letters* **13**, 100-105 (2012).

69 Radisavljevic, B. & Kis, A. Mobility engineering and a metal–insulator transition in monolayer MoS_2. *Nature materials* **12**, 815-820 (2013).

70 Ho, P. H. *et al.* Precisely Controlled Ultrastrong Photoinduced Doping at Graphene–Heterostructures Assisted by Trap-State-Mediated Charge Transfer. *Advanced Materials* **27**, 7809-7815 (2015).

71 Lagarde, D. *et al.* Carrier and polarization dynamics in monolayer MoS_2. *Physical review letters* **112**, 047401 (2014).

72 Kaushik, N., Karmakar, D., Nipane, A., Karande, S. & Lodha, S. Interfacial n-Doping Using an Ultrathin TiO_2 Layer for Contact Resistance Reduction in MoS_2. *ACS applied materials & interfaces* **8**, 256-263 (2015).

73 Zhang, S. *et al.* Extraordinary photoluminescence and strong temperature/angle-dependent Raman responses in few-layer phosphorene. *ACS nano* **8**, 9590-9596 (2014).

74 Fei, R. & Yang, L. Strain-engineering the anisotropic electrical conductance of few-layer black phosphorus. *Nano letters* **14**, 2884-2889 (2014).

75 Qiao, J., Kong, X., Hu, Z.-X., Yang, F. & Ji, W. High-mobility transport anisotropy and linear dichroism in few-layer black phosphorus. *Nature communications* **5** (2014).

76 Yuan, H. *et al.* Polarization-sensitive broadband photodetector using a black phosphorus vertical p–n junction. *Nature nanotechnology* **10**, 707-713 (2015).

77 Song, H. *et al.* Highly Anisotropic Sb2Se3 Nanosheets: Gentle Exfoliation from the Bulk Precursors Possessing 1D Crystal Structure. *Advanced Materials* (2017).

78 Du Y. Qiu G, Wang Y, et al. 1D van der Waals Material Tellurium: Raman Spectroscoy under Strain and Magneto-transport[J]. *arXiv preprint* arXiv:1704.07020, 2017.

79 Lanzillo, N. A. *et al.* Temperature-dependent phonon shifts in monolayer MoS_2. *Applied Physics Letters* **103**, 093102 (2013).